Utrecht University

Faculty of Science
Debye Institute

Measuring Size and Electrophoretic Mobility of Sub 100 nm Particles by Single Particle Tracking

Master thesis

Peter N.A. Speets

Experimental Physics

main supervisors

Dr.ir. Sanli Faez
Nanolinx

Prof.Dr. Allard P. Mosk
Nanolinx

daily supervisor

Dashka Baasanjav
Nanolinx

January 2019

Abstract

Single particle tracking of diffusing nanoparticles can be used to measure their size distribution. In this project gold nanoparticles and products from disaggregating fibrils both ranging from 30 nm to 100 nm were sideways illuminated by a laser. The emitted Rayleigh scattering from the particles was recorded with camera and used to localise the particles. The same technique was used to measure the electrophoretic mobility of 100 nm particles. It was found that, although it is difficult to find the exact size distribution, general differences between different size distributions can be measured. The measurement of the electrophoretic mobility by single particle tracking using this technique induces electro-osmotic effects that are highly dependent on the electric charge, shape and size of the measurement device itself.

1 Introduction

The goal of the experiments for this project is to characterise the size and electrophoretic mobility distributions of a sample of known or unknown nanoparticles or proteins. For good understanding of various (biological) equilibrium reactions knowledge about the size and charge is a good method to separate different species [1], especially if changes of different distributions can be measured over time. Single particle tracking of the diffusion of nanoparticles due to Brownian motion is not new. Nanoparticle tracking experiments are in such a way established, it made its way to undergraduate experimental practical courses[2]. In fact, study of particle movement has been done as early as 1908, by Jean-Baptiste Perrin in this studies to prove the atomic nature of matter[3]. The size of a particle follows directly from its diffusion from the Stokes-Einstein equation: $\langle r^2 \rangle = 4Dt \propto \frac{1}{a}$, with the mean squared displacement (MSD) $\langle r^2 \rangle$, the diffusion constant D and the diameter a. To distinguish different species and to be able to quantitatively estimate the amount of particles within a sample, single particle tracking is promising technique compared to dynamic light scattering (DLS), since DLS is more sensitive towards larger particles. Even traces of larger particles within a sample make it difficult to find smaller particles using DLS. Using single particle tracking instead my give a more reliable particle size distribution.[4].

The research described in this thesis both builds upon the many experiments on the Brownian motion of particles to find the size distribution of a sample of nanoparticles[5], but also consists of pioneering work to use single particle tracking and image processing to find the distribution of the electrophoretic mobility of a sample. The charge of proteins is commonly measured using gel electrophoresis[6]. A drawback of gel electrophoresis is that it cannot be done in the solvent in which a chemical reaction takes place. A simpler method is to directly apply an electric field in any suspension of particles to track the response of the particles. In this project different approaches have been tried to find a reliable and reproducible method to measure the size distribution and electrophoretic mobility by means of particle tracking or image processing. This thesis describes the most successful approaches, as well as some earlier work in the appendices.

In this project particles suspended in deionised water were illuminated from the side. A laser coupled into an optical fibre was used as a light source. The tip of the fibre was placed in the suspension of colloids. The Rayleigh scattering from the particles was imaged using a microscope. With this technique particles as small as 40 nm could be imaged.

The use of microfluidic devices has become commonplace in chemistry. Complicated microfluidic lab-on-a-chip devices have even be used to mimic electric devices[7, 8]. Simple devices are still being used to do science. With a seemingly simple components like paper and sticky tape these experiments are sometimes considered to be part of a so called “frugal science” movement[9]. A well known example of “frugal science” is for instance the Foldscope project[9]. The work described in this thesis may be considered to be following the “frugal science” movement, since the experimental parts are mostly build with simple materials, like sticky tape, laminating plastic and polyacrylate.

2 Theory

2.1 Brownian motion

The diffusion of particles performing Brownian motion is first described by Einstein[10]. In his paper Einstein describes that the diffusion of a spherical particle is linear in time. The Stokes-Einstein equation is as follows:

$$D = \frac{k_B T}{3\pi\eta a} \tag{1}$$

Were D is the diffusion constant, k_B the Boltzmann constant, T the temperature, η the viscosity of the solvent and a the diameter of the particle. Traditionally the derivation of the Stokes-Einstein equation starts with the Langevin equation:

$$m\dot{\vec{v}} = -m\xi\vec{v} + \vec{f}(t) \tag{2}$$

Here m is the mass of the particle, $\vec{v}$ the velocity of the particle and ξ a drag coefficient. This is the Stokes drag coefficient[11]:

$$\xi = \frac{6\pi\eta a}{m} \tag{3}$$

$\vec{f}(t)$ is a random force that acts on the particle. It is assumed that this random force applies in each direction in equal measure and has a white noise character, and has therefore $\langle\vec{f}\rangle = 0$ and no self correlation[12]:

$$\langle f_i(\tau) f_j(\tau')\rangle = 2G\delta_{ij}\delta_{\tau-\tau'} \tag{4}$$

The white noise character can be assumed, because the collisions of the particle with the solvent molecules are on a much smaller time scale as any method the diffusion of the particle can be measured. If only the friction force $-m\xi\vec{v}$ is taken into account, the speed of the particle exponentially decays over time: $\vec{v}(t) = \vec{v}_0 e^{-\xi t}$. If the random force is retained, the velocity of the particle is the integral over the history of the random force and the drag that any velocity gain the particle might have gotten from the random force[12]:

$$\vec{v}(t) = \vec{v}_0 e^{-\xi t} + \frac{1}{m}\int_0^t \vec{f}(\tau) e^{\xi(\tau-t)}\,\mathrm{d}\tau \tag{5}$$

Since we are not interested in the particle speed at a given time t, but rather the mean squared displacement. The average squared speed $\langle\vec{v}(t)\cdot\vec{v}(t)\rangle$ can be calculated. By squaring and averaging Equation 5 and removing all cross terms that go to 0 when averaged or go to 0 in the limit $t \to \infty$ and inserting Equation 4, the solution of the Langevin (Equation 2) equation looks like[12]:

$$\langle\vec{v}^2\rangle = \frac{6G}{m^2}\int_0^t e^{2\tau-2t}\,\mathrm{d}\tau = \frac{3G}{m\xi} \tag{6}$$

A spherical particle has three degrees of freedom in space, so through the equipartition theorem for the thermal energy, the speed of the particle is: $\vec{v}^2 = \frac{3k_B T}{m}$. This means that the strength of the random force $\vec{f}$ is $G = mk_B T\xi$. Using this expression in Equation 6, this gives:

$$\langle\vec{v}(t)\cdot\vec{v}(t')\rangle = \frac{3k_B T}{m}\, e^{-xi(t-t')} \tag{7}$$

The above equation can be used to calculate the mean square displacement of the particle. The displacement of the particle is the integral of the history of its velocity, so for a particle starting at the origin, the displacement is[12]

$$\langle \vec{r}^2(t) \rangle = \int_0^t \int_0^t \langle \vec{v}(\tau) \cdot \vec{v}(\tau') \rangle \mathrm{d}\tau \, \mathrm{d}\tau' = \frac{6k_B T}{m\xi} \left(t + \frac{e^{-\xi t} - 1}{\xi} \right) \tag{8}$$

Together with the Stokes drag coefficient (Equation 3), the mean squared displacement becomes for time scales much larger than ξ^{-1} the well known expression:

$$MSD = 6Dt \quad \text{with} \quad D = \frac{k_B T}{6\pi\eta a} \tag{9}$$

This is a good approximation, since for a gold nanoparticle of diameteter 100 nm, the ballistic drag time ξ^{-1} is $\approx$ 6 ns, which is much smaller than the exposure time of 18 ms. Because this experiment is performed on two dimensional diffusion of the particles, the mean squared displacement actually becomes:

$$MSD = 4Dt \tag{10}$$

2.2 Tracking errors

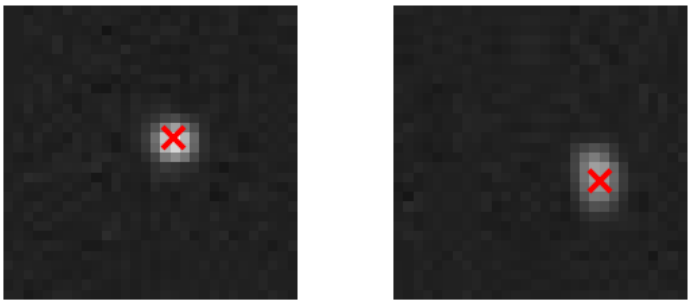

(a) Without motion blurring (b) Motion blurred particle

Figure 1: Example particle features with and without motion blurring. The motion blurring is an additional contribution to the localisation error.

The error in the localised position causes an offset in the measured MSD[13–15]. This error has a feature has multiple sources. The accuracy of the localisation algorithm is limited by the signal to noise ratio (SNR) and the camera pixelisation. This is the static part of the localisation error. During the experiment the SNR of a particle may vary, as it moves in and out of focus, so the localisation error is not the same in each frame or for each particle. The accuracy in the particle detection is also limited by the non-zero exposure time, since the detection algorithm locates the particle somewhere between start position and the end position of a particle during the exposure time. This is the dynamic error. An example of the latter kind of error is shown in Figure 1. These two errors are distinct, because for small particle tracks the static error increases the measured MSD, while a large dynamic error reduces it. This can be intuitively understood that the static localisation error acts like an additional random displacement of the particle, whereas the dynamic error is larger for larger random particle displacements, and always in the direction of the previous particle location. This means that for the latter example the measured MSD is lower.

X. Michalet [13] states estimates of the tracking error caused by both the static localisation error, and the error caused by motion blurring. This section is based on this paper and helps to understand the systematic errors found in simulated data. An expression for the localisation error that takes into account motion blurring is stated below:

$$\sigma = \sigma_0 \sqrt{1 + \frac{D\tau}{s_0^2}} \tag{11}$$

Here σ is the total localisation error, σ_0 the standard localisation error without motion blurring, D the diffusion constant of the particle, τ the exposure time and s_0 the width of the detected feature. For a Gaussian shaped particle s_0 is standard deviation of the particle profile. Taking these errors into account in Equation 10, the mean squared displacement of one step between frames and the offset caused by both errors is given by:

$$MSD(t) = \left(4\sigma^2 - \tfrac{4}{3}D\tau\right) + 4Dt \tag{12}$$

These systematic errors are further investigated using particle tracking of computer simulated data.

2.3 Screening effect of a charged surface

A charged surface in a liquid disperses the ions in the liquid. The ions in the liquid will cancel the electric field of the charged surface, negating the effect of the charged surface, because the ions that have similar charge as the surface will be repelled, whereas the ions that have opposing charge will be attracted to the charged surface. This behaviour is described by the Poisson-Boltzmann equation that equates the thermal motion of the particles with an electric potential. Giving a Boltzmann weight to the concentrations of the negative and positive ions in the liquid gives the following equation for the concentration of the positive and negative ions at position x: $c_\pm(x) = c_0 e^{\mp \beta e \phi(x)}$ with c_0 the bulk ion concentration of each of the two species and ϕ the electric potential[1]. The change of the electric potential is described by the Poission equation: $\nabla^2\phi = \frac{-\rho(x)}{\epsilon_r \epsilon_0}$ with ρ the difference between the positive and negative ions: $\rho = c_+ - c_-$. Using the Bolzmann weights in the Poission equation for the charge density ρ yields the Poisson-Boltzmann equation [1]:

$$\nabla^2\phi = \frac{2Zec_0}{\epsilon} \sinh\left(\frac{Ze}{k_B T}\right) \tag{13}$$

Here Z is the ionic strength of the ions in the liquid, which is 1 for deionised water, ϵ is the electric permittivity of the liquid and e the unit charge. If the potential at the surface ζ is small compared to the thermal energy $k_B T$, the system satisfies the Hückel limit: $Ze\zeta \ll k_B T$. The right hand side of the Poisson-Boltzmann can be Taylor expanded. In this case the electric field in the liquid will exponentially decrease with the distance from the surface. This is the Debye-Hückel approximation and is a textbook example of what the decay of the potential from a charged surface looks like[1]:

$$\begin{aligned} \phi(x) &= \zeta e^{-x/\lambda_D} \\ \text{With: } \lambda_D &= \sqrt{\frac{\epsilon k_B T}{2c_0 (Ze)^2}} \end{aligned} \tag{14}$$

The decay length of this potential is the Debye length λ_D. The Debye length is is often used as a measure of the size of the cloud of screened ions around a nanoparticle. The Debye length is not dependent on properties of the surface or particle, but is a property of the solvent. The Debye length in deionised water is slightly less than a micron, see Figure 2, but is usually of the order of magnitude of tens of nanometres. The concentrations of the ions in the solvent are [1]:

$$c_\pm = c_0 \left(1 \mp \frac{Ze\zeta}{k_B T} e^{-z/\lambda_D}\right) \tag{15}$$

To find the ion density in the liquid, the chemical potential is assumed to be constant, which must be the case in equilibrium. The chemical potential for the concentrations of the positive and negative ions is [1]:

$$\mu_{\pm} = \mu_0 + k_B T \ln\left(\frac{c_{\pm}(x)}{c_0}\right) \pm Ze\phi(x) \tag{16}$$

Because the chemical potential is constant, gradients of the last two terms are equal. Integration of this differential equation yields an expression for the ion density per species [1]:

$$c_{\pm} = c_0 \exp\left(\frac{\mp Ze\phi(x)}{k_B T}\right) \tag{17}$$

This equation, together with a solution for the electric potential of the Poisson-Boltzmann equation (Equation 13), the Gouy-Chapman solution stated below, a correction on the purely exponential decay of the ion distributions can be calculated [1].

$$\phi(x) = \frac{2k_B T}{Ze} \operatorname{arctanh}\left(\tanh\left(\frac{Ze\zeta}{4k_B T}\right) e^{-x/\lambda_D}\right) \tag{18}$$

For the Debye-Hückel approximation and the Gouy-Chapman solution, the ion density and electric potential are plotted for deionised water and a ζ potential of 50 mV in Figure 2.

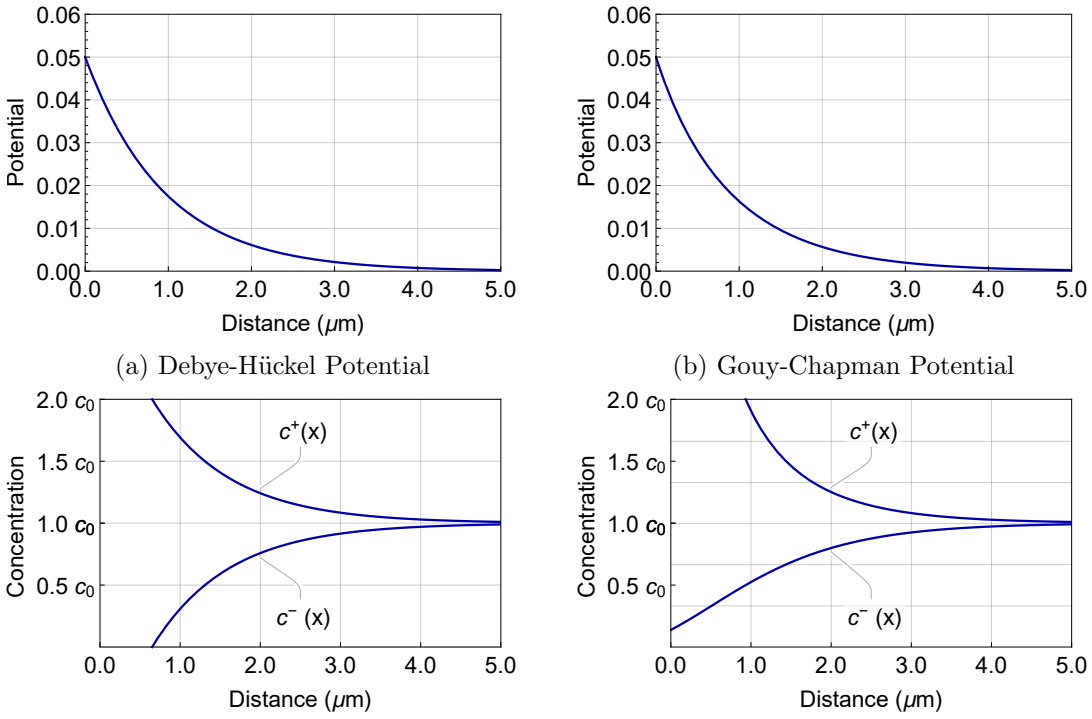

(a) Debye-Hückel Potential

(b) Gouy-Chapman Potential

(c) Debye-Hückel Concentration

(d) Gouy-Chapman Concentration

Figure 2: Examples of the potential and ion concentrations of the Debye-Hückel approximation and the Gouy-Chapman potential for a flat negatively charged surface in water. The bulk ion concentration c_0 for these plots is 10^{-7} mol/l and the ζ-potential of the surface 50 mV, which corresponds to a Debye length of $\lambda_D = 0.95$ μm. The Gouy-Chapman potential in Figure b is very similar to the exponential decay in Figure a, although the Debye-Hückel limit, $ze\zeta \ll k_B T$, is not satisfied. In Figure c and d the concentrations of the ions are plotted for deionised water with $[H^+]$ and $[H_3O^-] = 10^{-7}$ mol/l. In both models the screening effect cancels the influence of the surface charge on the potential and the concentration difference after approximately 5 μm.

2.4 The electric double layer

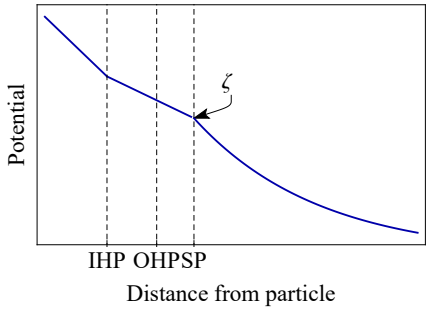

Figure 3: Sketch of how the electric potential ϕ develops over distance from the surface of the particle. Until the *inner Helmholtz plane* (IHP) the ions are not screened, but are stuck to the surface of the particle. The ions in the solvent between the IHP and the *outer Helmholtz plane* (OHP) are considered to be in a diffuse layer where the ions are screened, but bound to the colloid. The ions in the diffuse layer can move in or out of this layer and are located between the OHP and the *slip plane* (SP) . The ζ potential is the electric potential at the slip plane [16].

The ion cloud that negates the charge around a particle described in the previous section, only applies to the screening of the ions in the solvent. Close to the particle, the way the ions position themselves is dependent on the distance from the particle. A sketch of how the electric potential develops is shown in Figure 3. Very close to the surface of the particle the ions are tied to the surface because of the strong electric forces. The decrease of potential with distance to the particle is not due to the screening of the ions, but due to a layer of ions that are stuck to the surface of the particle. The layer between the two Helmholtz planes is the diffuse layer where particles are closely tied to the particle, but have the freedom to diffuse in and out of the diffuse layer. For electrophoresis the diffuse layer and the slip plane are important, because the colloids and their bound (strongly or loosely) ions are are considered to move as a single system when an electric field is applied. Therefore the outer plane of this layer is called the slip plane. The potential at the slip plane is the ζ potential. This is the charge of the colloid that is measured in electrophoretic measurements [16]. The particle and its double layer can, however, polarize under an electric field, causing frequency dependent behaviour for frequencies of the electric field much higher than used in this research project [16]. In this respect, the electric potential might be considered a DC potential with the low frequencies used in this project. Any frequency dependency described in Section 5 is not due to polarisation of the ion cloud around the particles.

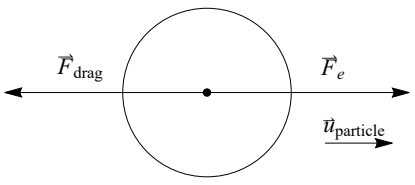

Figure 4: Sketch of force balance once the particle has reached its terminal velocity. The Stokes drag force is equal to $\vec{F} = -6\pi\eta a\vec{u}$ with η the viscosity of the solvent, a the radius of the particle and $\vec{u}$ the velocity of the particle. This must be equal to the electric force $\vec{F}_e = q\vec{E}$.

In Figure 4 the force balance is sketched. Because the drag force is linear in the velocity of the particle and the ions around the particle are approximated to be tied to the particle in the double layer, the velocity of the particle should be linear with respect to an applied potential. Equating the Stokes drag force (Equation 3) and the electric force applied to the particle gives an expression for the velocity of the particle [1]:

$$\vec{u} = \frac{Q}{6\pi\eta a} = \mu E \tag{19}$$

With μ the electrophoretic mobility. This means that the electrophoretic mobility is essentially a measure for the charge of the particle, so it can be used for differentiation between species. If the electrophoretic mobility is written in terms of the ζ-potential, the mobility becomes[16]:

$$\mu = \frac{\epsilon_r \epsilon_0 \zeta}{\eta} = \frac{Q}{6\pi\eta a} \tag{20}$$

This is the Helmholtz–Smoluchowski equation.

2.5 Electro-osmosis

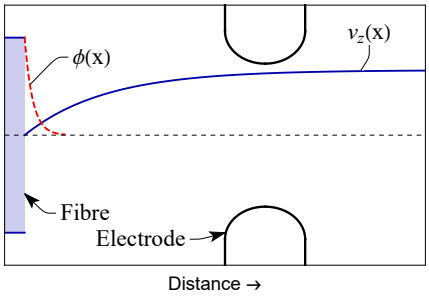

Figure 5: Sketch of an electro-osmotic flow of an infinite charge plane that is used as a toy model to describe electro-osmotic effects when the electrophoresis experiment is performed close to the optical fibre. If the fibre is described as an infinitely large charged surface, even with a short Debye length, it can have an effect on the flow rate of the solvent on a distance much larger than the Debye length.

To see how the charge on the surface of the fibre can effect electrophoresis experiments that are performed 100 micron from the fibre, this section describes a toy model of the electro-osmotic flow that is caused by the potential between the electrodes and the surface charge of the fibre. This model assumes the fibre to be an infinitely large charged surface with a potential described with a Debye-Hückel approximation of its surface charge and with a homogeneous field in the z-direction, parallel to the surface. Both assumptions are not satisfied in experiment. The screened potential and resulting velocity profile are sketched in Figure 5. Although this model yields unphysical results, it can provide insight on how an electro-osmotic flow influences electrophoresis experiments.

To calculate the electro-osmotic flow rate, a good starting point is the modified Navier-Stokes equation to contain the effect of a potential on a charged fluid as stated by H. Bruus [1]:

$$\rho\left(\partial_t \vec{v} + (\vec{v}\cdot\nabla)\vec{v}\right) = -\vec{v}p_{ext} + \eta\nabla^2\vec{v} - \rho_e \nabla U_{ext} \tag{21}$$

Here ρ is the density of the solvent, $\vec{v}$ the velocity profile, p_{ext} and external pressure, η the viscosity of the liquid, ρ_e equilibrium the ion density in charge per volume and U_{ext} the applied potential between the electrodes. For a steady state solution, with liquid flow only in

the direction of the applied electric field between the electrodes and without external pressure, only the last two terms are taken into account. The simplified equation is [1]:

$$\eta \frac{\partial^2 v_z}{\partial x^2} = \rho_e \frac{\partial U_{ext}}{\partial z} \tag{22}$$

Here the charge density ρ_e is the difference in in ion concentrations given by Equation 15. The ρ_e in Equation 22 can be written in terms of the Debye-Hückel potential ϕ of Equation 14 by using that by differentiating twice ϕ in x gives $-\rho_e/\epsilon$. Together with the electric field $E = -\Delta U/\Delta z$ with Δz the distance between the electrodes is given by[1]:

$$\frac{\partial^2 v_z(x)}{\partial x^2} = \frac{\epsilon E}{\eta} \frac{\partial^2 \phi(x)}{\partial x^2} \tag{23}$$

Integrating over z twice and using a no slip boundary condition at the surface of the charged plane ($v(0) = 0$), a solution of this equation is, with ζ the ζ-potential of the charged wall:

$$v_z(x) = \frac{\zeta \epsilon E}{\eta} - \frac{\epsilon E}{\eta} \phi(x) \tag{24}$$

With the potential ϕ given by Equation 14: $\phi(x) = \zeta e^{-x/\lambda_D}$. The reason this result is unphysical is that this flow does not go to 0 for $x \to \infty$, but to $\frac{\epsilon \zeta E}{\eta}$. It is however instructive to see that an electro-osmotic flow can affect electrophoresis measurements even at a much longer distance from the fibre than the Debye length. Also, if both the fibre and particles in the solvent have the same charge, the electro-osmotic flow is opposite to the electrophoretic movement of the particle. Because the maximum velocity of the electro-osmotic flow is reached in a few Debye lengths from the fibre and the velocity should eventually decay to 0 for large x, the most significant effect of the electro-osmotic flow on the electrophoretic measurements is closest to the optical fibre considering the typical length scales of the setup.

2.6 Rayleigh scattering

The particle are illuminated from the side and the scattered light from the particles is imaged. The Rayleigh equation describing the scattering is given by [17, 18]:

$$I = I_0 \frac{1 + \cos^2 \theta}{2d^2} \left(\frac{2\pi}{\lambda} \right)^4 \left(\frac{n^2 - 1}{n^2 + 2} \right)^2 r_p^6 \tag{25}$$

With I_0 the incident light, θ the scattering angle, d the distance to the particle, λ the wavelength of the light and n the refractive index of the particle. The radius of the particle is r. This means that for particles with different sizes the ratio between the detected intensities is r_1^6/r_2^6.

3 Methods

This section describes both experimental methods and the analysis of the experiments. Some of the techniques described in this part could not be used for the main results in this thesis. In those cases the the results will be summarised in the appendix.

3.1 Flow cell

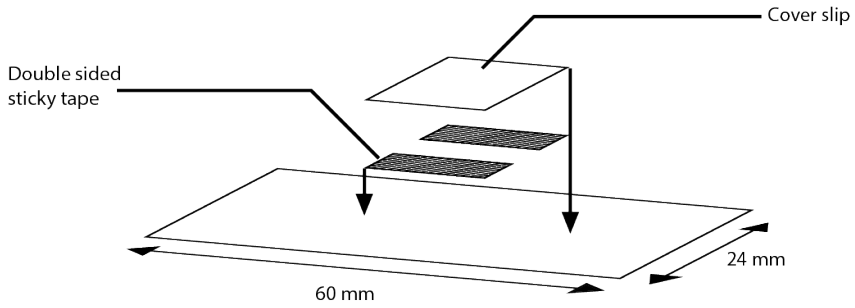

Figure 6: The channel used for particle tracking of the biological sample and the gold nanoparticles.

3.1.1 Microfluidic channel

Of the many flow cell and electrode configurations tried, two setups were used for the reported measurements. For the size distribution of gold nanoparticles an optical fibre glued on a microscope slice would suffice. Such a very simple configuration, however, leaves the droplet open, which may cause drift in the sample caused by air flow. For this reason for the measurements on fibrils a closed flow cell was used. A sketch of this flow cell is shown in Figure 6. The channel consists of a piece of a microscope slide as cover slip attached to another microscope slide with two strips of double sided sticky tape. To make the channel watertight, thorough cleaning of both microscope slides is required. The sticky tape will stick to the glass for the entire measurement if the microscope slide and the cover are cleaned well. The cleaning is done by flushing the microscope slides twice with subsequently ethanol, isopropanol and demineralized water. After flushing the demineralized water droplets are blown from microscope slides or to the side of the glass with nitrogen, taking the grease and dirt with it. This is the reason the last step is water, since ethanol and isopropanol evaporate on the glass instead of being pushed to the side by the flow of nitrogen. The double sided sticky tape is attached to the small top cover and attached to the microscope slide. To attach the cover to the microscope slide, some pressure is required. This makes it easier to use a piece of the ticker microscope slide instead of the thin cover slips. The sample is made on a aluminium foil sheet to prevent dust from the table to attach on the clean glass surface. Using paper instead would leave too much dust and paper fibres on the glass. After the channel is complete, an optical fibre is attached to the microscope slide with UV glue. UV glue has the advantage that it does dry when the fibre is being aligned.

This channel is used for the diffusion measurements of 30 nm and 40 nm gold nanoparticles (GNP) and disaggregation products of fibrils. A closed sample with illumination from the top caused too much light to scatter on the walls of the channel itself as described in Appendix C.

3.1.2 Manipulable electrodes

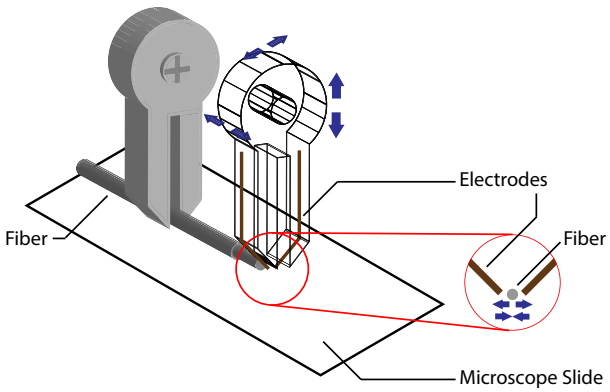

Figure 7: Sketch of the manipulatable electrodes. The electrodes can move in the two axial directions and in the lateral direction. The distance between the electrodes can be varied. The height of the optical fibre can be varied, but it needs support from a spacer. This spacer can be a cover slip. In this experiment a 15×15 mm^2 #1 cover slip is used.

The electrodes for most of the measurements on electrophoretic mobility are shown in Figure 7. Two key-shaped holders are attached to manually manipulable stages. On one holder two electrodes are glued and the other holder clamps an optical fibre. The fibre is not glued, but clamped to be able to reuse the fibre. The two key-shaped holders are cut with a laser cutter from acrylic glass. The two stages that move the holders can move in all three directions. The electrodes are glued to the key-shaped holders. The electrodes initially make an angle between each other as can be seen in the magnification in Figure 7. The electrodes are vertically aligned by pressing them on the microscope slide. The electrodes are aligned in the horizontal direction by moving and toughing them with tweezers or a toothpick. The alignment of the electrodes can be fine-tuned by pressing them with left-over optical fibre clamped between the beams of the other stage before the optical fibre is attached. The distance between the electrodes can be varied by moving the two beams of the holder closer together by tightening or loosening a bolt that is pressing the two beams of the holder together. The electrodes are copper or platinum wires of about 200 μm that are separated by pulling the wire apart. This process may result in relatively smooth rounded tips, but also in very asymmetric tips. Before attaching the electrodes the wire tips are checked under the microscope. A bright-field image of the used electrodes is shown in Figure 8. The electric field around the electrodes should approximately be a dipole field. If the FOV is centred between the electrodes, the field is almost homogeneous, as shown in Figure 47 in Section 5.

The measurements done using the manipulable electrodes were performed at 135 μm, 265 μm and 390 μm from the optical fibre and a separation of the electrodes of 212 μm.

Because the fibre is flexible and there is a few centimetres distance between the holder of the fibre and the electrodes, the fibre will always stick to the microscope slide if a droplet is applied. To prevent this the distance from the optical fibre can only be changed by a spacer. In this case a #1 15×15 mm cover slip is used as as spacer.

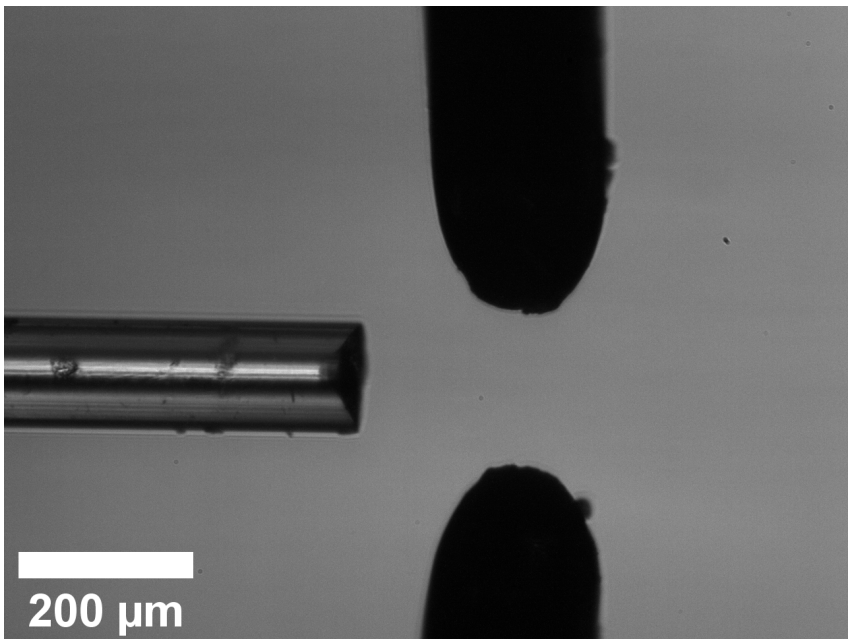

Figure 8: Brightfield image of the electrodes and the fibre. Both the fibre and the electrodes can move in all three directions. The distance between the electrodes can be varied.

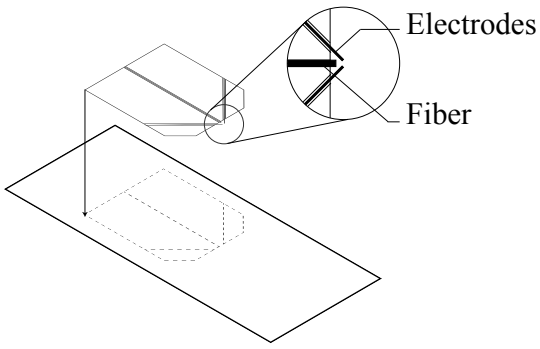

(a) A sketch of the sample. The sample consists of a plastic holder for the optical fiber and the electrodes that is placed onto a microscope slide.

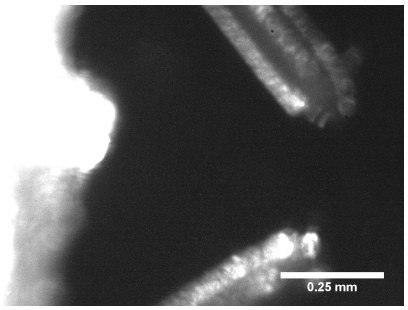

(b) Image of the electrodes (gray) and the optical fiber (white).

Figure 9: Fixed electrodes. Contrary to the manipulable electrodes, this electrode design has electrodes that make a 90° angle with respect to each other. The electrodes are made from copper wire.

3.1.3 Fixed electrodes

Some measurements were performed using fixed electrodes (see Appendix D). The fixed electrodes are attached as shown in Figure 9. Just as the previous setups the sample is illuminated from the side with an optical fibre. Both the optical fibre and the copper electrodes are glued with UV glue to a plastic spacer made from laminating plastic. In the laminating plastic slids are cut to align the fibre and the electrodes. The plastic spacer with the optical fibre and the electrodes is glued to a microscope slide. The slids cut into the plastic do not offer enough precision to align the fibre and the electrodes, so after the glue dried, the wires are gently moved with a toothpick into place. The laminating plastic is about a few hundred micron thick and the electrodes are located 525 μm from the fibre and the distance between the electrodes is 275 μm. This means that the measurements using the fixed electrodes were done at a larger distance from the optical fibre than with the manipulable electrodes. The platinum electrodes give much better result and do not dissolve into the water. A measurement using these electrodes is shown in Appendix D.

3.2 Characterizing images

Although the characterization of the imaged data is informative by itself, information about the signal to noise ratio (SNR) and the size of the particles is also required to create simulated data with the same properties. To obtain the SNR of the images, a method similar to the method described by by Savin and Doyle[19] is used. As signal the average maximum pixel value of the detected features is used. The noise is the standard deviation of all background pixels, which are distributed as a Gaussian distribution[20]. The average pixel value of the background is the backlevel. Proper background subtraction negatess the backlevel, so only the noise is considered. The SNR is the ratio between these values. The background pixels are obtained by convolving the raw image data with a kernel with a size similar to the features in the frame. This is the apparent radius of the imaged particles. This convolved frame is subtracted from a blurred image. All pixels in the subtracted image that are below a threshold are considered background. This frame is binarised for one last processing step. To filter out the tails of the visible particles from the background pixels and to compensate for the Gaussian blur, the binarised image is dilated with a radius the same as the apparent radius. The SNR of the brightest particles is 37, but the average over all particles gives a SNR of 9. The average SNR is so low, because a lot detected particles are out of focus.

3.3 Testing the triggering of the function generator

For the measurements of the electrophoretic mobility, the acquisition script of the computer triggers the camera to image and to give a signal to the function generator. The delay between the start of the exposure of the camera and the pulses given by the function generator is tested by using function generator as a DC source for an LED light. The light of the LED is captured by the camera on different exposure times for three different cases how the LED is triggered: when the LED is continuously on, when the LED is triggered by the camera and when the LED is off for background correction. Using the offset in the x-direction of the fits in Figure 11a , the measured trigger lag time is 2.2 ms, which is too long for immediate triggering, since this value is not much smaller than the exposure time of 8 ms of a frame if the camera operates at 120 FPS. Each measurement on electrophoretic mobility is done in such way that the full movement of the particle is captured by making the exposure time larger than the period of the movement of the particle. For this estimate immediate response of the LED is assumed.

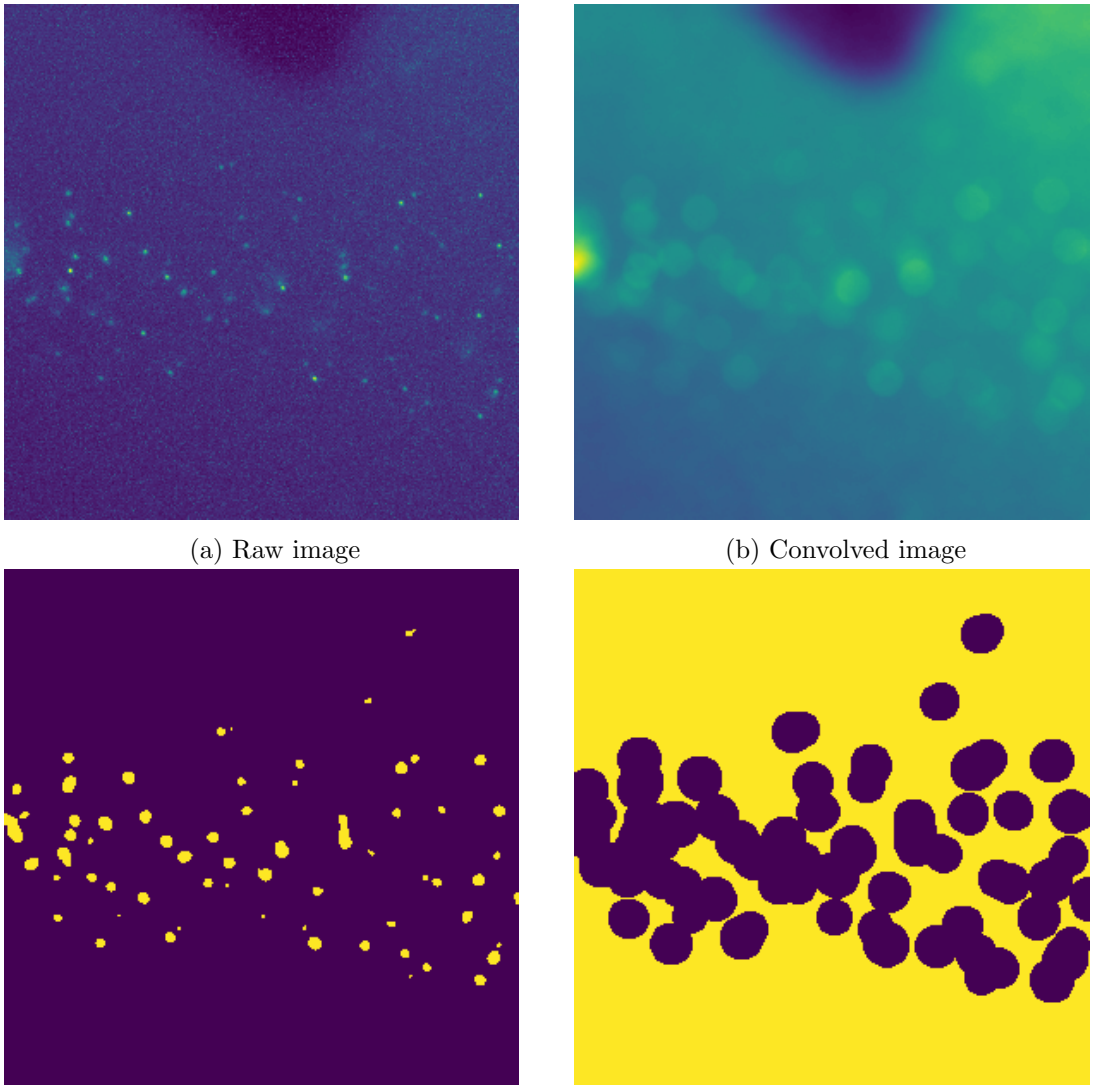

(a) Raw image

(b) Convolved image

(c) Binary image

(d) Dilated binary image

Figure 10: To obtain the background pixels from the images to calculate the SNR, the frame in Figure (a) is convolved with a constant disk shaped kernel. Subtracting this convolved image from a Gaussian blurred image and imposing a minimum threshold pixel value a binary image as in Figure (c). If this binary image is dilated with a radius similar to the kernel size with which the image in Figure (b) is convolved, the features in Figure (c) are enlarged, so the background pixels are obtained.

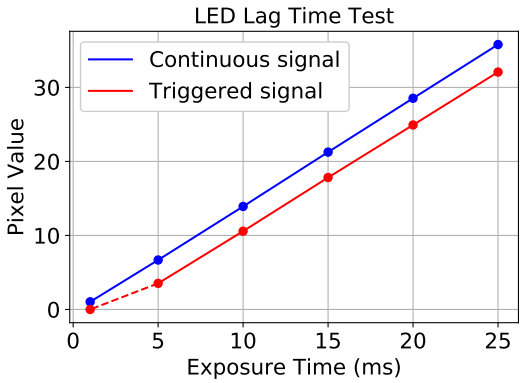

(a) Average pixel values for a continuous signal and a triggerd signal.

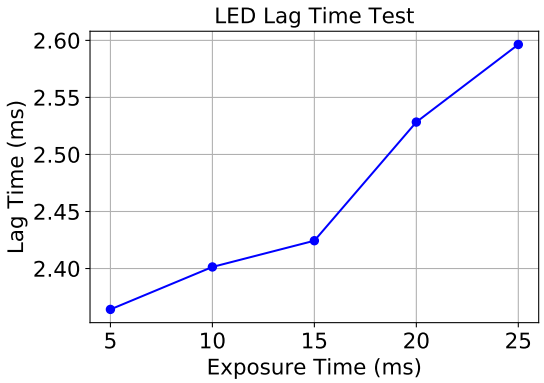

(b) Lag time for different exposure times.

Figure 11: In the left image the average pixel values of an image illuminated by a continuous burning and a triggered LED are plotted. The offset between both fits is 2.2 ms. The dashed line is not taken into account, since the point through 0 ms does not give any information about the triggering. In figure on the right an estimate of the lag time is plotted based on the difference between the average pixel value of the triggered signal and the continuous signal.

3.4 Imaging

The imaging is done on the samples described in section 3.1 using a Zeiss Axiovert 135 microscope and a 407 nm laser (ThorLabs LP405-SF30 fiber-pigtailed laser) at 25 mW[21]. The light is coupled to an optical fibre and led to the sample. The coupling with the optical fibre results in some losses, so the power output in the sample is lower than 25 mW. The camera that is used for each experiment is a Basler daA1280-54um. For the measurement of the diffusion constant exact knowledge of the camera frame rate is required. Therefore the camera frame rate was not set to a larger frame rate than 55 FPS[22]. Because the sample is different in each measurement, the measurement is done with different settings, as described in the relevant subsection. The channel used for the size distribution of the GNP and the fibrils was flushed multiple times before a new sample was introduced. The flushing was done by applying deionised water on one size of the channel and pulling it though the channel by sucking it up into a piece of paper. If the measurement did not require an electrode, the measurement was performed in a channel to prevent drift of the sample. The measurements on electrophoresis are done with an open droplet, thus increasing the risk of drift caused by air flow.

3.4.1 Size distribution of GNP

The size distribution of the gold nanoparticles is determined by the Brownian motion of the particles. From the displacements of the particles the size distribution is determined by using the Stokes-Einstein equation (Equation 10). The samples that were used are 1.0 μl 1 OD sample of 30 nm gold nanoparticles diluted with 3 ml deionised water and 22.2 μl 1 OD sample of 40 nm gold nanoparticles diluted with 3 ml deionised water. From these bulk samples 1 μl of the 30 nm gold nanoparticles sample and 2.22 μl of the 40 nm gold nanoparticles were diluted with another 300 μl of deionised water for the measurement. The sample with the combination of both particles consists of 10.0 μl 30 nm gold nanoparticles and 100.0 μl 40 nm gold nanoparticles. The amount of 40 nm particles in the combined sample is therefore higher tnan the number of 30 nm particles. For each measurement 10 000 frames were imaged, but divided in videos of 2000 frames to save memory.

3.4.2 Size distribution of Fibrils

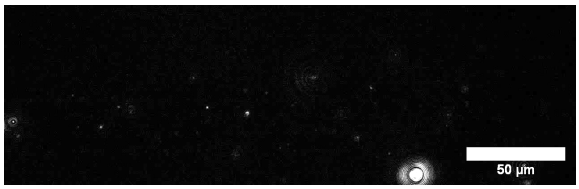

(a) Example of the 0 h sample

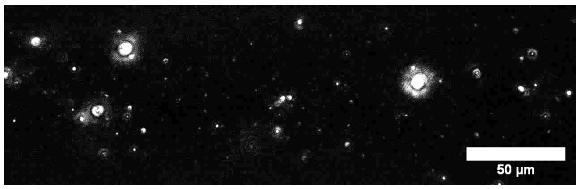

(b) Example of the 24 h sample

Figure 12: Examples of imaged frames. The left image is a frame from the sample that could not react and the right image is a frame from a sample that reacted for 24 hours. The particles smaller than visible in the image were tracked. This distribution of small particles changes over time to smaller particles. The brightness of these images is increased for better visibility.

The size distribution of tau fibrils, mixed with molecular chaperones and ATP, is determined as function of time. The samples were made and provided by Gerarda van de Kamp[23]. The reaction time between the fibrils, chaperones and ATP was limited by freezing the sample. The imaged samples were 8 samples that were frozen after a number of hours and 2 control samples. In general the same procedure is followed as for the GNP. The sample was flushed by deionised water multiple times. The amount of deionised water used for flushing is arbitrary, but flushsing was done at least five times, but often much more. Whether the channel was clean, was judged from the number of particles visible in the sample. It was not possible with this method to remove each particle from the channel, but the number of particles that were left in the channel is much lower than are introduced in the sample. An example of how the imaged fibrils look like when imaged with in the microscope is shown in Figure 12. The number of times the channel needs to be flushed should not be as high as 10 to 20 times. Probably dust and sample residue at the entrance of the channel were reintroduced by the first flushing attempts, increasing the number of flushes required to fully empty the channel. After the channel was flushed 10 μl of the sample was introduced on the side of the channel with the shortest distance to the tip of the fibre, so the particles could diffuse into the channel. The particles are almost immediately visible despite the distance between the entrance of the fibre, but it required several minutes for the drift to stabilize. The samples were imaged for 10 000 frames and split in videos of 2000 frames.

3.4.3 Electrophoretic mobility

The measurements of the electrophoretic mobiltiy of particles were done with the manipulable electrodes described in Section 3.1.2 in an open droplet. The measurements were done with 100 nm GNP. To separate electro-osmotic effects and to investigate the frequency response of the particles in the droplet, the particles were imaged on several distances from the optical fibre. The distances between the electrodes and between the electrodes and the fibre cannot be easily accurately selected in advance, so the distances between the tip of the fibre and the electrodes was determined after the measurements based on a bright field image of the electrodes and fibre. The potential on the electrodes was applied with a function generator that was triggered from the camera just before imaging. After receiving the trigger signal the function generator sends a few sinusoidal pulses with an amplitude and frequency depending on the experiment. The number of pulses was chosen such that the field will be applied during the entire exposure of the frame. The exposure time of a measurement is 0.17 s. Although a larger exposure time increases the signal, the effect of Brownian motion becomes too large. Between each frame, the imaging and electric pulse stops for at least one second. This is a one second explicit pause in addition to the time the script needs to save the data to the disk. This is to prevent the creation of bubbles caused by the electrolysis of water at the tips of the electrodes. In the experiments

in which a copper wire was used instead of a platinum wire, this is also to prevent the electrode from disintegrating. These processes also take place when the experiment pauses for a second each measurement, but the system has time to recover. A continuous signal, whether it is AC or DC, can already cause bubbles at 3 V.

For the experiments with the platinum electrodes a much larger parameter space was explored, but the measurement time was decreased to 100 videos of 20 frames. This is done to prevent moving of the focus over time and accumulating dust, that might happen on the time scale of about one hour and because it is impossible to explore a large parameter space with long measurements. The used objective for the video based measurements was a 10× 0.25 NA air objective. The magnification is lower than in the experiment with diffusing particles to allow the use of a higher frame rate, because the camera could only image faster than 55 FPS if a fraction of the available pixels were used. Because this feature is not specified in the specifications[22], this feature was not used for the measurements on Brownian diffusion. Since an accurate frame rate of the camera is less important for the measurements of the electrophoretic mobility, the camera could operate at 120 FPS instead of 55 FPS. The results of the video measurements are described in Section 5. The FOV is covering the region between the electrodes, which is for the used objective all pixels the camera can image at 120 FPS. In this case all imaging was done with a image size of 400×400 pixels.

For the experiment with the copper wires two long measurements of 2000 frames were done. The experiments with the copper wires did not yield any results as described in Appendix B.

3.5 Analysis

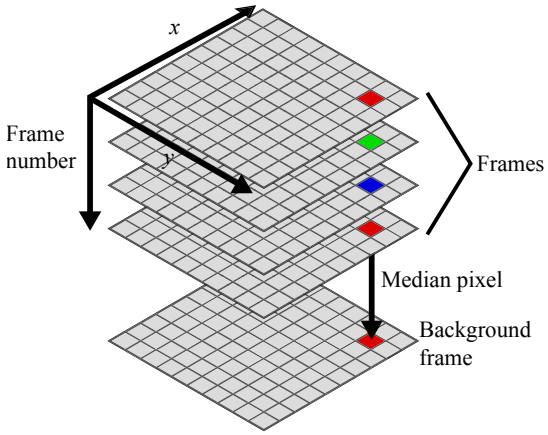

Figure 13: The static background was calculated by taking the median pixel value at a x and y position over the whole video. This background frame was subtracted from each frame before analysis.

Before the particles can be tracked, the static background of the images was subtracted. The static background was calculated by subtracting the median pixel value from the measured frame stack. An example is sketched in Figure 13. This is necessary, because stray light from the laser scatters on the microscope slip and the electrodes. Subtracting the background also diminishes the effect of dust on the camera and optics.

3.5.1 Tracking algorithm

For the tracking of the particles the Crocker and Grier algorithm [24] was used. The Crocker and Grier algorithm algorithm implementation that was used, is the Trackpy[25] package for Python. This package is used for all experiments on diffusive particles. The algorithm first performs a Gaussian blur on the image with radius 1. It subsequently selects all pixels that

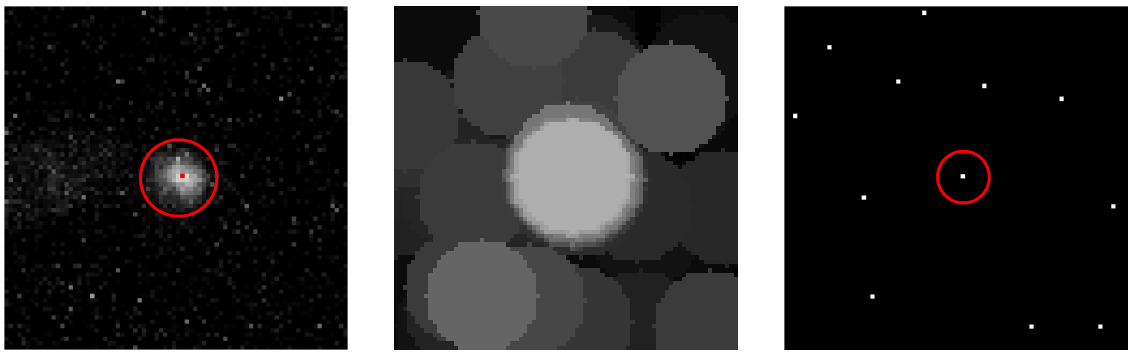

(a) Raw image (b) Dilated image (c) Candidate pixels

Figure 14: The raw image in Figure 14a contains a particle that is detected by subtracting the dilated image in Figure 14b from an image blurred with a Gaussian with radius 1. All local maxima will be zero and all other pixels will be negative. The pixels which are local maxima are shown in Figure 14c. If the sum of pixel values of the pixels surrounding the candidate pixels is large enough, it is considered a particle. Only the candidate pixel surrounded by the red circle in Figure (c) has enough bright pixels nearby. The centre can be further refined by using the centre of mass.

have no brighter neighbours within a diameter w, with w roughly equal to the apparent diameter of the particle. The selection of the bright pixels was obtained by subtracting the gray dilated image from the blurred image. Each non-negative pixel is a candidate pixel. To filter candidate pixels, the sum of pixel values within the disk of radius w is calculated. If the total intensity is large enough, it is retained. This sum of pixels values is chosen such that it is as low as possible, to also track dimmer particles. If a few background features are falsely selected as particles, it can be filtered out later by imposing a minimum displacement of the particles. Subpixel accuracy is obtained by using the centre of mass of the particle. The centre is altered with a distance $\epsilon_{x,y}$ according to[24]:

$$\begin{pmatrix} \epsilon_x \\ \epsilon_y \end{pmatrix} = \frac{1}{m_0} \sum_{i^2+j^2 \leq w^2} \begin{pmatrix} i \\ j \end{pmatrix} A(i_0 + i, j_0 + j) \tag{26}$$

With $A(i, j)$ the pixel value at pixel i, j and m_0 the sum of each pixel within the disk of radius w.

Each located feature in a frame is linked to a feature in a next frame based on proximity and intensity. If a particle cannot be linked, it can skip up to 3 frames such that particles can move in and out of FOV, in and out of focus or being covered by other particles. Each track must include at least 20 frames. This biases towards larger particles, since smaller particles are too difficult to track. The minimum root mean square displacement is 0.05 px and the maximum 10 px. Particles with an eccentricity larger than 0.5 are filtered out. Hardly any particles are filtered out by the limits on eccentricity displacement, since these caps are very lenient. To compensate for drift in the sample, the average motion per frame per frame is subtracted from the tracks in the experiments that use the Brownian motion of the particle.

To fit the diffusion constant, a moving window of 5 data points are fitted to $MSD = 4Dt^n$ and the average diffusion constant of these windows is used for the analysis. The fitting with a window is done to decrease inaccuracy induced by the fitting[13]. To obtain the diameter of particle from te diffusion constant, the Stokes-Einstein equation is used: $4Dt = \frac{2k_BT}{2\pi\eta a}$, in which k_B is the Boltzmann constant, T the temperature, η the viscosity and a the diameter of the particle. For T the value of 293 K is used and for the viscosity 10^-3 Pas. For plotting of the distributions, the tracks are weighted by their track lengths.

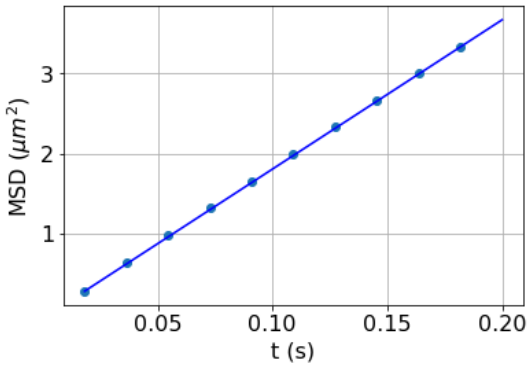

Figure 15: Example of a fit of the first 10 images. For this fit all measurements on all particles are used. The data points of the individual particles have a much larger spread. The linear behaviour justifies the use of the Stokes-Einstein equation (Equation 10).

3.5.2 Analysis of electrophoretic mobility

The measurement of the electrophoretic mobility of the particles is done using different methods. The analysis of the electrophoretic mobility of the particles can be divided in two approaches: analysis of the traces in a single frame that is exposed as long as the length of the applied electric pulse and the single particle tracking in a video of the particle moving in an electric field. The first method has the advantage that it can be used for much smaller exposure times and a larger magnification, but the second method is easier to implement. In this project the two methods were tested, but only the analysis of the video yielded reliable results. The results of the analysis of the videos is described in Section 5. The problems with fitting the long exposed images are described in Appendix B.

3.5.3 Detection of particle traces

The electrophoretic mobility of a particle in an electric field is proportional to the length of the trace that the particle leaves in an image due to motion blurring, or the peak to peak amplitude of the particle motion in a video. This section describes the method used obtain particle traces from overexposed images. To obtain the length of a particle trace, similar methods as the previous section are used, based on the methods of Savin *et al.*[19]. Almost all parameters in this section are arbitrary and changed such that most traces are detected. The settings selection criteria are used to filter out the features that are dust, aggregates or particles with badly defined traces. Some features, like parts of a ring from the Airy pattern of out of focus particles, are difficult to separate from particle traces by using this analysis program, so a manual check of the selected features is still required.

From the imaged frames the background is subtracted with the same method as for the diffusing particles. After the background is subtracted, each frame is subsequently analysed. To detect the possible features, the image is blurred with a Gaussian and then convolved by a disk with a disk about the same size as twice the apparent radius of the particle. This value might change per experiment, but a typical value is 30 px. This blurred image is subtracted from the raw image. Any nonzero value that is at least a minimum threshold value, is treated as potential feature. To fully detect the middle part of the trace where the velocity of the particle is the highest, the threshold value is as low as possible. For further processing the image is binarised. The signal of the particles can be quite low, since the signal is spread over a larger area. The analysed frames have therefore a low SNR. Therefore noise is detected as feature. To filter the peaks caused by noise, an opening and closing operations with typical disk sizes of 10 px are applied to the binary image. The closing operation makes features that are closely to

each other connect. This step is necessary for the images measured with a low AC frequency, since the signal between the tips of the traces can be quite low. After the closing operation an opening operation is applied to filter all features that consist of only a few pixels. The binary image is dilated with a disk with the size of the apparent radius to fully crop the particle. If the detected feature passes filters on size, intensity, aspect ratio and proximity to the border, the feature is selected as particle trace.

This method selected too much false positives as particle traces (Appendix B). The most common false positives were parts of the Airy rings around out of focus particles. False positives can be avoided by manually selecting the particles from the data. For this purpose a graphical script was written with which the particle traces could be manually selected. The disadvantage of this method is the long time it takes to review all data and to select all particle traces.

The length of trace is determined by calculating the full width at half maximum (FWHM) of the detected trace for the measurements done with a copper electrode, or a weighted linear fit of the particle trace. Since a sine wave AC signal is used, the electrophoretic mobility is given by:

$$\mu = \pi f l / E \tag{27}$$

In this equation f is the frequency of the potential and l the length of the trace and E the electric field. The size of the electric field is taken to be the applied potential divided by the distance between the electrodes. To compare the different measurements, E is approximated by the applied potential divided by the distance between the electrodes. The field between the electrodes should approximately be the shape of a dipole. Therefore the FWHM is not necessarily a good method to obtain the trace length. For data obtained with platinum electrodes a weighted linear fit of the particle traces that were manually cropped from long exposed images was tried. This method however also proved unreliable, because the best fit was only part of the cases along the long axis of the particle trace.

3.5.4 Single particle tracking of particles in an electric field

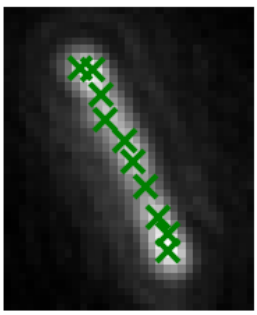

Figure 16: Example of all detected particle points in a small video of 20 frames. In this example all frames are combined to form a single image. The crosses mark the detected positions. The measured track length is the largest distance between the detected particle positions.

To cope with the problems described in the previous section, the electrophoretic mobility is not measured by analysing the particle traces of a long exposed image, but using the Grocker and Grier algorithm for single particle tracking on small videos of 20 frames. The particles are detected by using the same methods as used for the diffusive particles, except that the minimum track length is 20 frames and the drift of the particles cannot be subtracted. An example of a video particle trajectory is shown in Figure 16. The measured particle length is the maximum distance between the detected positions in the particle track. The use of particle tracking of a

video to obtain the particle trace has two disadvantages compared to the measurement of the trace length of long exposure images: the resolution is limited to the movement of the particle within a frame and the detection of the centre of the particle is less accurate due to motion blurring. For these reasons the applied electric field is a sine wave. Because the particle will spend more time at the tips of the track the resolution is more than the track length divided by the number of frames per video and the motion blurring at the tips. The places in the track that matters for the track length, the localisation is more accurate. In the example of Figure 16, the crosses are placed closer together at the tips of the trace. The reported electrophoretic mobility is calculated using the same methods as described in the previous section: $\mu = \pi f l/E$ with f the electric frequency and l the distance of the trace and E the electric field. The advantage of the use of video instead of long exposed images is that more information about the motion of the particle can be obtained such as drift. For long exposed images this would be indistinguishable from a larger trace length.

3.6 Simulation

To estimate the uncertainty and systematic error in the tracking algorithm, simulated data is generated and tracked using the same analysis as imaged data. The simulated data consists of randomly displaced Gaussian intensity distribution. The intensity and size of the particles is chosen to be the same as the imaged data for 100 nm particles. The particle is randomly displaced in the x and y direction with a Gaussian probability distribution. This Gaussian displacement in each direction follows Equation 28, with $\sigma = \sqrt{2 * D}$ with D the diffusion constant in pixel squared per time step Δt. Each frame is divided by 100 time steps, so at 55 FPS the time step is about $\Delta t = 182\mu$s. Each time step the Gaussian distribution of the particle is added to a single frame, such that the effect of motion blurring is simulated. In each frame a constant background and Gaussian noise is added with the same spread as calculated from the imaged data in the previous section (Section 3.2). This was chosen to be a SNR of 30. The difference in real and measured mean square displacement is a systematic error in the tracking algorithm and the spread in the data of the random error.

$$P(\Delta x, \Delta y) = e^{-\frac{(\Delta x, \Delta y)}{2\sigma}} \tag{28}$$

The simulation is run for a simulated 100 nm with $0.23\,\mu$m/px for track lengths varying from 10 to 250 frames and 100 runs for each track length. The total number of data points is is thus larger for the longer track length, but this does not make a difference for the spread or systematic error.

4 Results of Brownian motion experiments

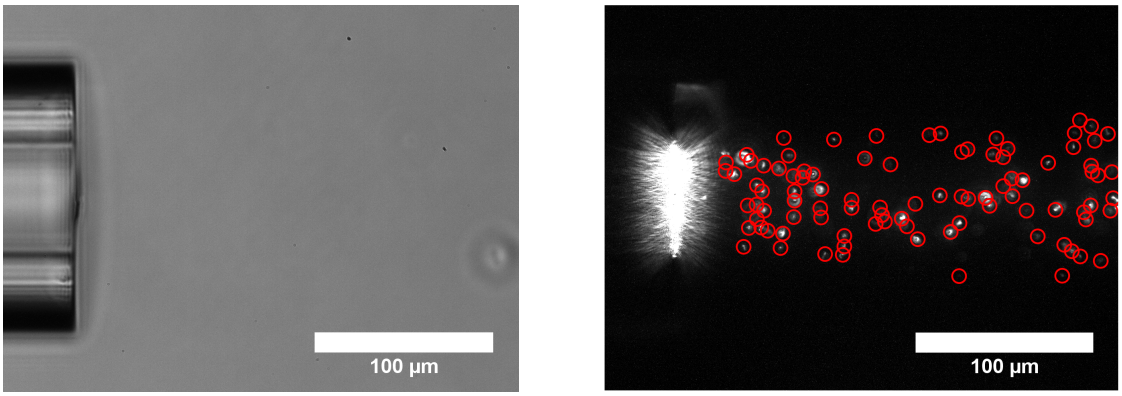

(a) Brightfield illumination (b) Laser illumination

Figure 17: Example of light scattering on particles in the sample. Figure (a) is a brightfield image of both the optical fibre and the sample of gold nanoparticles. In the right image, the brightfield illumination is turned off and the particles are illuminated by the laser from the optical fibre. The encircled particles are the features deteced by the tracking software.

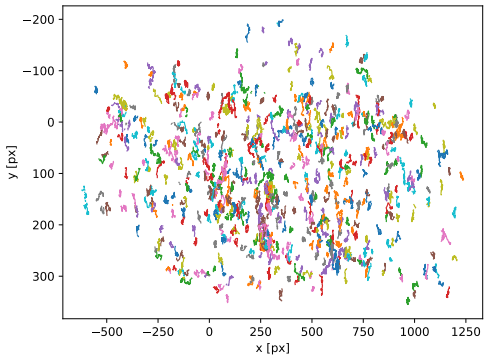

Figure 18: Example of linked trajectories of 40 nm gold nanoparticles. Each colour represents a different track.

(a) 40 nm GNP (b) Profile

Figure 19: Example of a particle and its profile.

Single particle tracking of fibrils or particles illuminated by the sideways positioned optical fibre is used to obtain an estimate of the diameter using the diffusion of the particles. An example of the detected features is shown in Figure 17, where the brightfield and laser illumination are compared. Linking the detected features in each frame gives tracks as in Figure 18. Such

a detected particle is shown in Figure 19. In this chapter the results of tracking experiments of diffusing gold nanoparticles and biological samples are discussed, as well as simulation results where the simulated particles were tracked by the same tracking algorithm as the gold nanoparticles and fibrils.

4.1 Simulation of diffusing particles

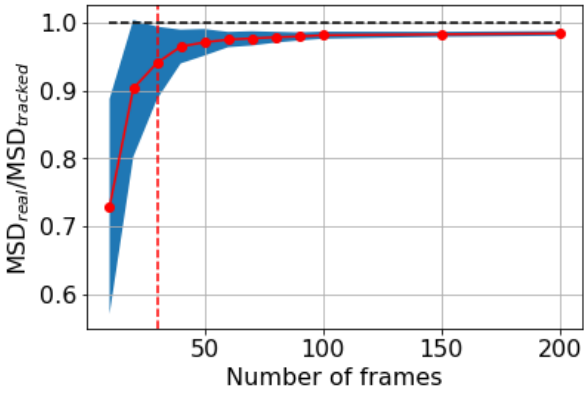

Figure 20: The simulated MSD divided by the tracked MSD of the simulated particle. The coloured area marks the standard deviation of this fraction. Not only the spread of the measured displacement is very high for short (< 30 frames) particle tracks, there is a systematic error to a larger measured particle displacement than the real displacement. This biases towards smaller particles.

The results of the particle tracking of simulated data is shown in Figure 20. The fraction of the real MSD obtained by simulated positions of a diffusing Brownian particle and the MSD calculated from the tracked positions are plotted. The measured MSD has a clear systematic error for for particles that are tracked for less frames than 50 frames. Particles tracked for 30 frames have a systematic error of their tracked MSD of 1.05 the real MSD. In Equation 12 the contributions of the static and dynamic error to the measured MSD are given. Since the measured MSD is higher than the simulated MSD, the static localisation error is higher than the dynamic error. This means that no improvement can be made on the localisation error by limiting the exposure time per frame. In all measurements the maximum exposure time per frame that the frame rate would allow, was used. For the reported results on Brownian motion, the minimum number of frames the particle was tracked is set to 30 frames.

4.2 Tracking of gold nanoparticles

Not only the diffusion of the particles gives information of the size of the particles, the intensity of the scattered light is proportional to a^6 with a the diameter of the particle. To characterise the experimental method, the size distribution of 30 nm and 40 nm gold nanoparticles is measured, together with a mixture of both particles. The size distribution is plotted in Figure 21. The mean particle diameters are 31.8 ± 0.18, 53.2 ± 0.48 and 66.0 ± 0.18 nm, with an error estimate calculated with $\sigma/\sqrt{N_{counts}}$. The diameter distributions are very broad, with standard deviations of 26.3, 42.4 and 23.8 nm. Since the distributions are asymmetrical, with a tail towards larger particles, the median diameter is perhaps a more justified value to represent the distribution. This also reduces the effect of outliers on the data. The medians are 21.3, 33.3 and 25.2 nm much smaller than the mean, because of the aforementioned long tail. In Figure 21 (b), a 68% interval is plotted around the median. In the sample with a mixture of

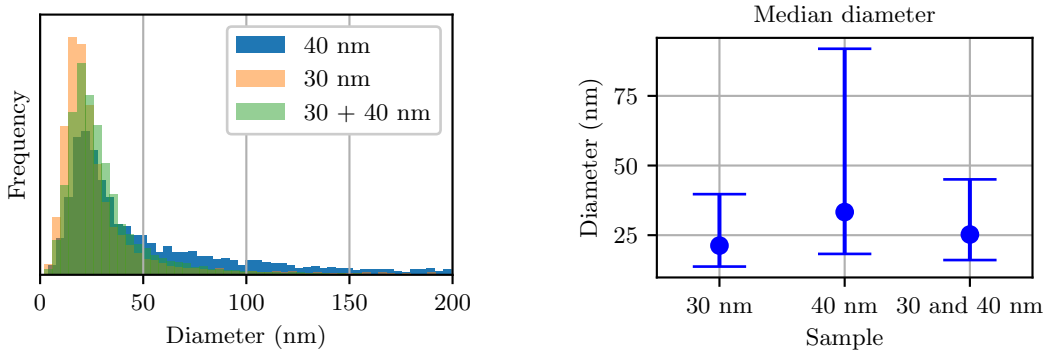

(a) Diameter (b) Median diameter

Figure 21: Histogram of the particle diameters as estimated from the particle tracking and the median particle diameters. The bars depict 68% of the particles around the median.

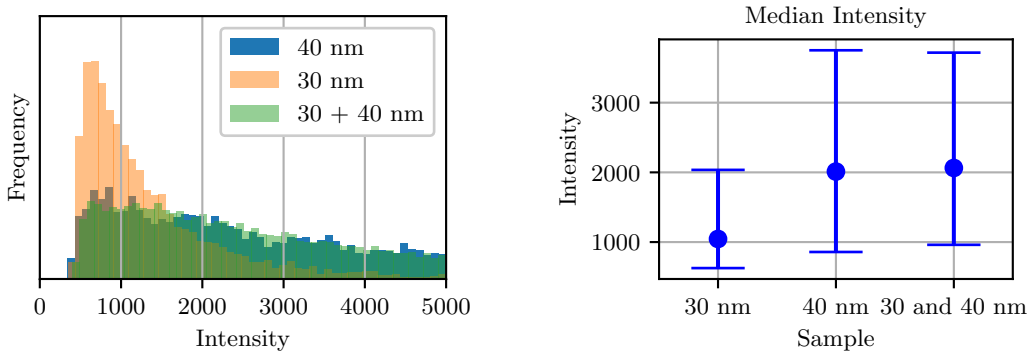

(a) Intensity (b) Median intensity

Figure 22: Histogram and median intensity. The intensity is the sum of all pixel values in a detected feature, averaged over its track.

particles, the 30 nm have a more distinct influence on the diameter distribution than the 40 nm particles, although the sample should contain approximately an equal amount of both species.

The intensity of the particles should correlate with the size of the particles, since the Rayleigh scattering law scales with a^6, so larger particles have a much higher signal. In Figure 22 the intensity of the particles is plotted. Compared to the diameter from the diffusion of the particles, the mixture of the two species is similar to the intensity distribution of 40 nm particles, instead of the 30 nm particles. Even though the intensity of the particles could be more sensitive to the diameter of the particles, the movement on the z-axis by diffusion is enough to bring the particle out of focus and therefore greatly increasing the spread in the intensity data. Another interesting thing is the correlation between the intensity and diameter. One would expect a positive correlation between the size obtained by diffusion and brightness of the particle. However, the density plots shown in Figure 23 show no correlation between both quantities. Calculating the Pearson correlation coefficient r yields -0.10, 0-.01 and -0.15 for the 30 nm, 40 nm and binary mixture respectively. The negative correlation is probably caused by very faint background features that survived the background subtraction, since these features have a very low intensity and very high diameter. Filtering these features however, would bias towards a detected distribution of smaller particles.

As shown in the previous section, an important parameter to reliably measure the diffusion constant by particle tracking is the track length. In Figure 24 the histogram and median

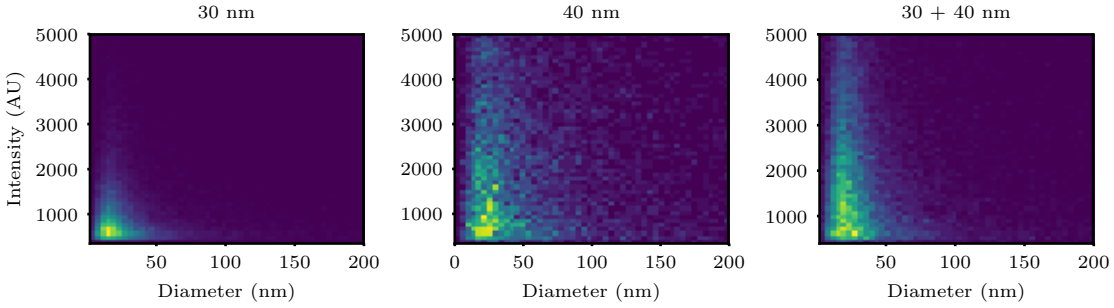

Figure 23: Heat plot of the diameter as determined by diffusion and the intensity of the particle. Because the particles move frequently in and out of focus, there is no correlation between particle diameter and the intensity. The points in the density plot form clusters around the measured diameter instead. The clusters are chopped by the minimum intensity filters.

track lengths are plotted. The track length distribution is chopped off for all samples by the requirement of a minimum of 20 frames, but for the 30 nm and binary sample only particles in the tail of the distribution are retained. Because the track length histogram is chopped for those two measurements, the median track length is artificially higher for those samples. The detection of background features, together with the chopped-off track length histogram suggests that particles of a diameter 30 nm are the lower bound of what can be detected with this setup reliably. In both diffusion and diameter, the two different species in the mixture could not be distinguished.

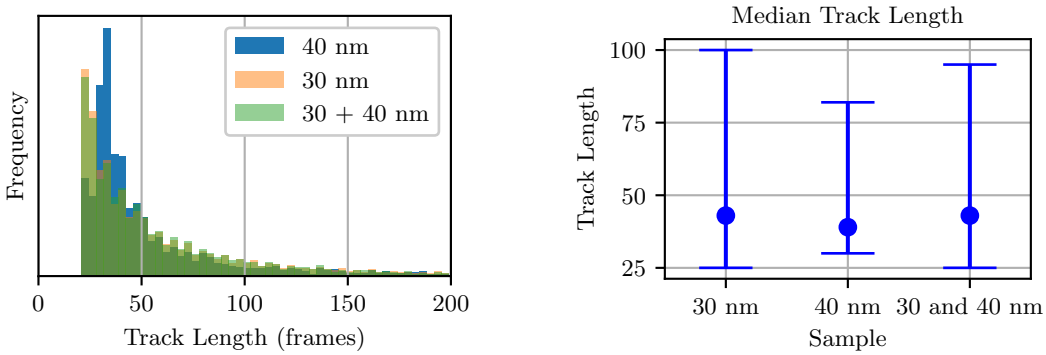

(a) Track length

(b) Median track length

Figure 24: Histogram of track lengths and the median track length. Because for tracks smaller than 20 frames the estimate becomes too unreliable, the histograms of 30 nm and 30 + 40 nm have a strong cut-off at 20 frames.

According to Equation 12, the measured MSD has an offset compared to the real motion of the particles due to random tracking errors and systematic errors due to motion blurring. To generate enough signal, all measurements are done with the longest exposure time possible at maximum frame rate of the camera. Since all detected features should be approximately symmetrical Gaussian distributions, the eccentricity of the features can indicate if the measurements have been affected by motion blurring. In Figure 25 the eccentricities of the detected features are plotted. The mean eccentricity is the largest for the 40 nm particles. The high eccentricity might explain the high spread in the diameter histogram of Figure 21.

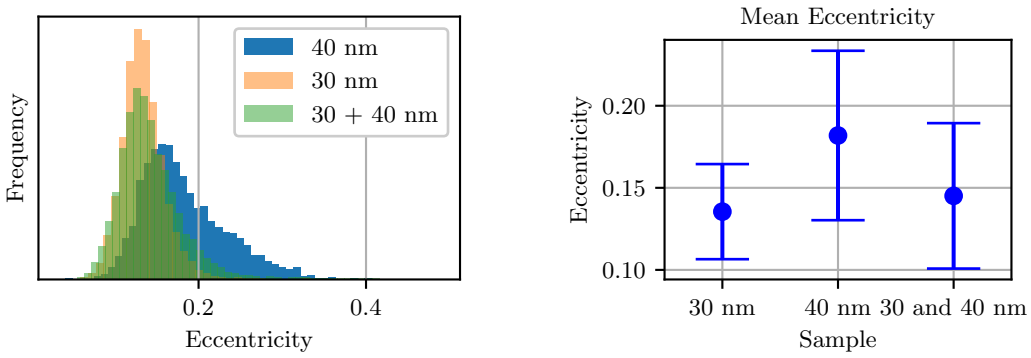

(a) Feature eccentricity

(b) Mean eccentricity

Figure 25: Histogram and mean eccentricity of the detected features as calculated by Trackpy[24]. The eccentricity distributions are approximately Gaussian, and therefore the mean, instead of median, is plotted in Figure (b).

4.3 Tracking of fibril residues

The setup and method described above is used to measure differences in the size distribution of a biological sample. The measured samples consist of tau fibrils that were allowed to react with molecular chaperones assisted with ATP[23]. The chaperones cut the fibrils in smaller particles that were measured. Seven samples with different reaction times ranging from 0 to 24 hours and two control samples were measured. The size histograms of the sample that was frozen before it could react, but where all the reactants were present and the sample that was allowed to react for 24 hours[23] are shown in Figure 26. The diameter shown in this figure is obtained through the Stokes-Einstein equation, which assumes spherical particles. The particles that are created by the disaggregation of the fibrils are not necessarily spherical, but the size distribution obtained through the MSD of the particle is a method to measure differences in particle size distribution between samples. The histogram clearly shows a shift to smaller particles when the fibrils were allowed to react for a longer time. The median particle diameter decreased in 24 hours from 192 nm to 135 nm. Not plotted is the mean diameter which changed from 195 nm to 166 nm. The process of the disaggregation of the fibrils happens gradually, with the exception of the sample that reacted for 8 hours. This sample both has a smaller diameter and smaller intensity that might be expected from the other data points, as can be seen in both Figure 26 and 27.

The particle count, as shown in Figure 28, does not change significantly below $t = 16$, but for the measurements of the $t = 20$ and $t = 24$ a much higher particle count is measured. The change in particle count and the diameter distribution is as expected, since the ATP assisted chaperones disaggregate the fibrils to smaller particles over time, therefore the average particle diameter decreased and particle count increased. The control samples have a much lower particle count and the sample of fibrils and ATP has a slightly higher particle diameter. No bright particles in the ATP sample are present. In all samples the scattering of the laser light was clearly visible by eye, but the particles of the ATP sample could only be seen by eye with larger camera gain settings.

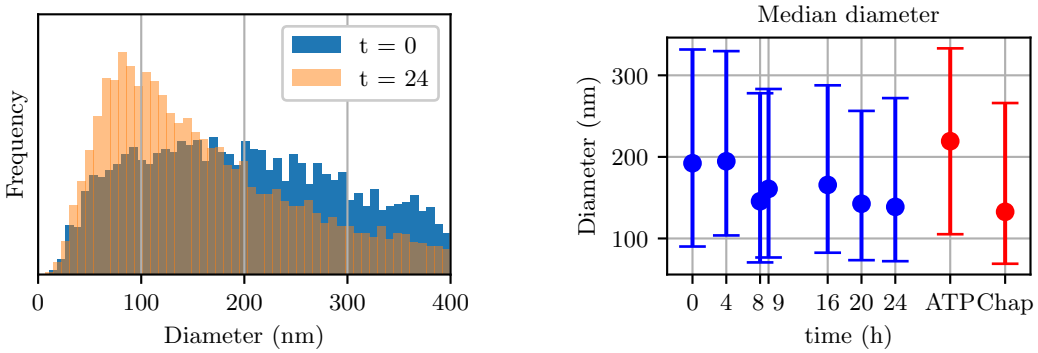

(a) Diameter

(b) Median diameter

Figure 26: Distribution of particle diameters. The sample in which the molecular chaperones have not reacted with the fibrils and the sample in which the chaperones were allowed to react with the fibrils for 24 h are compared. Over time the size distribution of sub micron particles shifts to smaller particles.

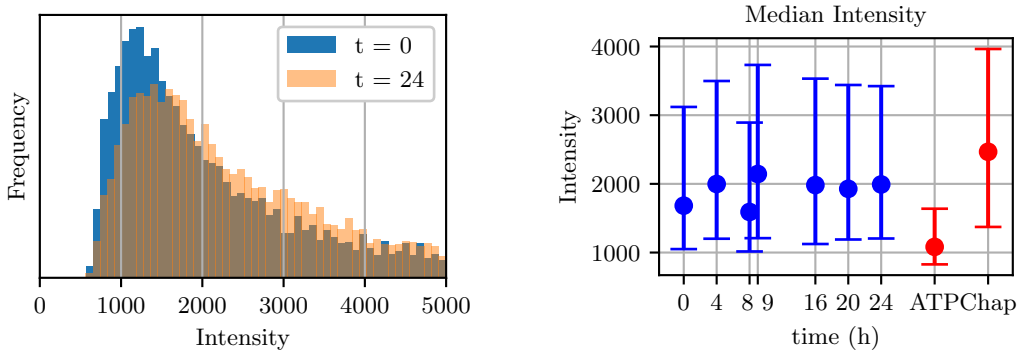

(a) Intensity

(b) Median intensity

Figure 27: The histogram of the intensities of the detected particles. The intensity does not differ much from the time samples, but the sample containing only fibrils and ATP have very dim particles.

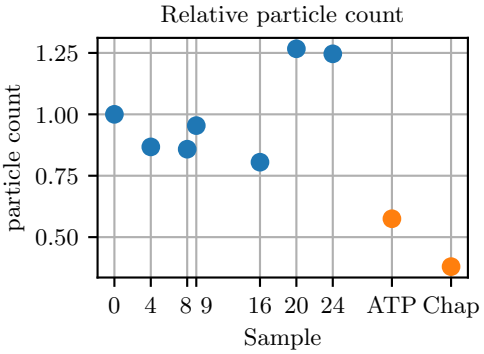

Figure 28: Particle count of the time measurements and the control samples. The particle count is normalised to the $t = 0$ sample. The particle count does not differ much for times lower than 16 hours, but the samples that have reacted for 20 and 24 hours have higher particle count, whereas the control samples have a lower particle count.

Because the results of the simulation suggest that the error of the measured displacement quickly drops below 50 frames, the minimum track length is set at 30 frames. Because the measured particles are small and move quickly out of focus, the histogram of the track length is clearly chopped-off. This suggest that the accuracy of the measurement could be the easiest improved by increasing the number of frames over which a single particle can be continuously tracked. The track length is for each measurement low with no clear exceptions among the measurements.

The eccentricity of the detected features is much higher than the measurements of 30 nm gold nanoparticles. The eccentricity is slightly higher than the eccentricity of the 40 nm gold nanoparticles. This is likely because proper calculation of the eccentricities of the particles requires enough signal. Since the particles that are created from the disaggregation process of the fibrils are on average larger than 40 nm, the eccentricity is higher. This also means that the tracking error due to a non-zero camera exposure time is higher than of the gold nanoparticles.

The combined result of the single particle experiment is plotted in Figure 31. This summarises the change in diameter distribution and median particle size. The distribution of the $t = 0$ sample looks similar to the ATP control sample and the $t = 24$ sample looks similar to the control sample with fibrils and chaperones. The full distributions are plotted in Appendix E.

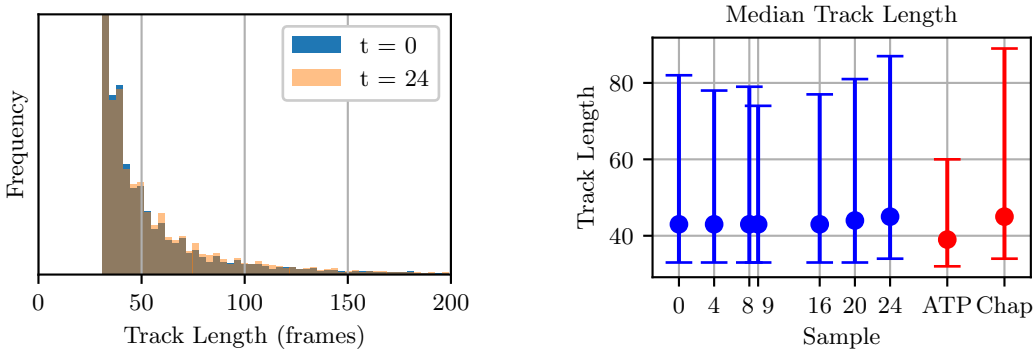

(a) Track length

(b) Median track length

Figure 29: Histogram of the track length and plot of the median track length. The histogram is clearly chopped off, meaning that the tracked particles move quickly out of focus. The sample containing fibrils and ATP has shorter track lengths than the other samples, which reflects its lower intensity.

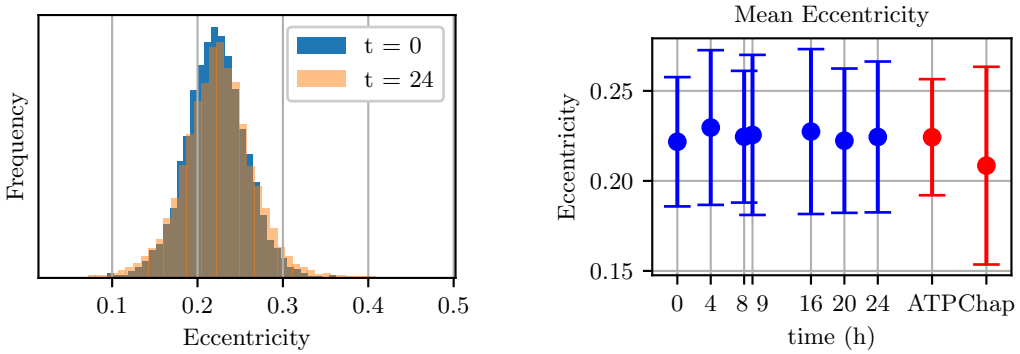

(a) Feature eccentricity

(b) Mean eccentricity

Figure 30: Histogram and mean eccentricity of the detected features. The eccentricity does not vary much among samples, but is much higher than the eccentricities shown in Figure 25.

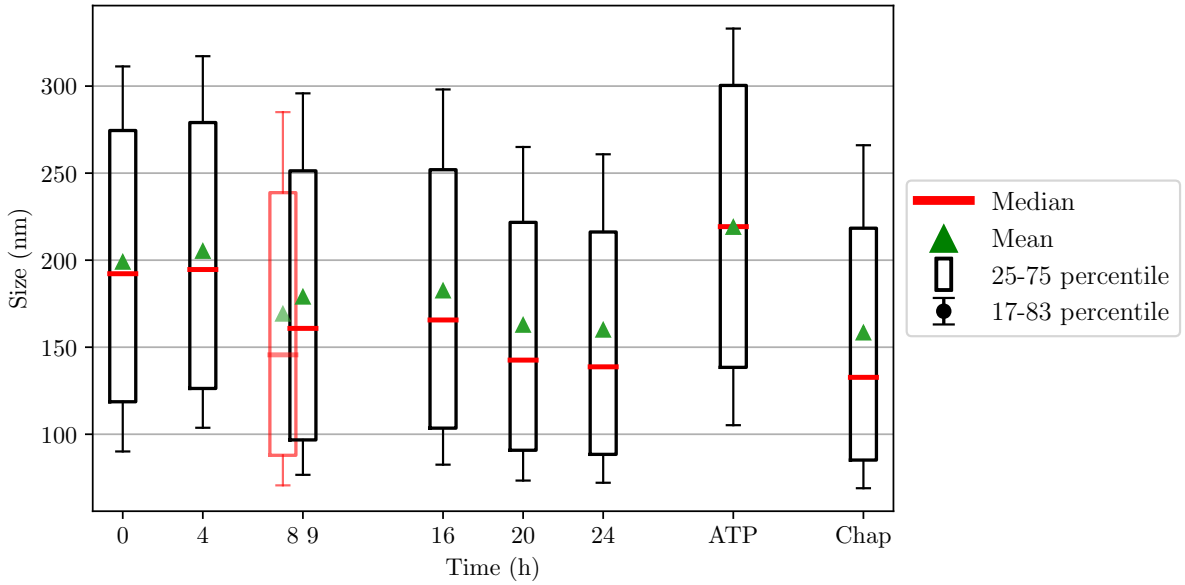

Figure 31: Box plot of the particle diameter distributions of the time measurements and the $t = 0$ and $t = 24$ sample compared with the two control samples. The diameter distribution of the $t = 0$ sample looks very similar to the sample with fibrils and ATP and the diameter distribution of the $t = 24$ sample looks similar to the control sample with ATP and chaperones. The measurement at $t = 8$ is an unexpected result in both the intensities of the particles and the size.

5 Results of Electrophoresis Experiments

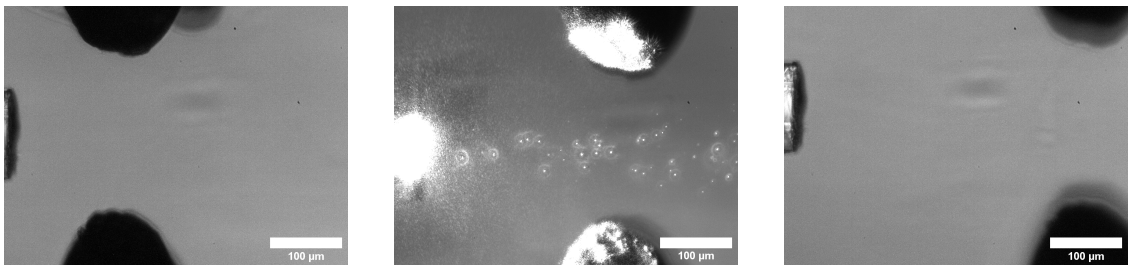

(a) 135 μm (b) 265 μm (c) 390 μm

Figure 32: The electrophoretic mobility is measured at three different positions from the optical fibre, at 135 μm, 265 μm and 390 μm. The electrodes are 212 μm apart. The distance between the particles and the microscope slide is in the order of 100 micron.

The response of 100 nm gold nanoparticles in an electric field is measured by tracking the particles between two platinum electrodes at three different distances from the optical fibre and at five different frequencies of the electric field. The optical fibre and the electrodes at the three distances are shown in Figure 32. The measurements were done at at 135 μm, 265 μm and 390 μm from the optical fibre with a 7.5 V AC potential of 10 Hz to 20 Hz. At 265 μm the measurement is repeated at 5 V. The electrodes are 212 μm apart. If the electrodes would be closer together, the light from the optical fibre wouldf scatter too much on the electrodes. In the middle image of Figure 32 the signal of the scattered light on the electrodes is already quite high.

An example of how the particles response to an electric field is given in Figure 33. The electrophoretic mobility is proportional to the length of the trace multiplied by the electric frequency.

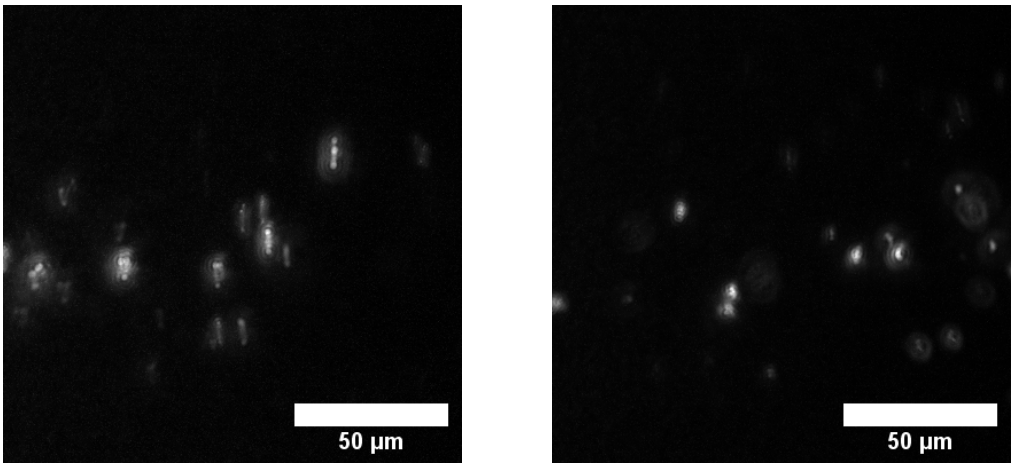

(a) 10 Hz (b) 20 Hz

Figure 33: Examples of particle traces of 100 nm gold nanoparticles in an electric field of 7.5 V at two different frequencies. The images were made by summing the 20 frames of a video.

5.1 Analysis of the collective motion

Calculating the mean displacements of tracked particles in the x and y directions of the particles moving in the electric field gives an average particle response plotted in Figure 34. For the calculation of the track lengths in Figure 35 the peak to peak height of the average movement the y direction is used. Because of the drift in the measurement, the peak to peak height is only calculated between the first maximum and minimum. This means that the drift in the sample does not affect the results in Figure 35 at the cost of accuracy. The drift in Figure 34 is not caused by a general liquid flow, but is caused by flow induced by the potential on the electrodes, judging from the results described in Section 5.2.

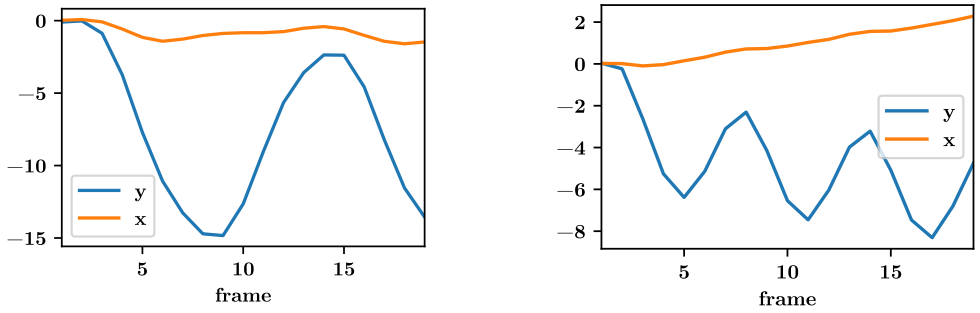

(a) 10 Hz

(b) 20 Hz

Figure 34: Collective average movements in the x direction and the y direction. Even though each measurement lasted only 0.17 s, the drift of the sample is clearly present. The electrodes in in Figure 32 seem aligned but there must be a small misalignment in the electrodes, because the drift in the x direction also has a response to the electric frequency.

The particle track length plotted in Figure 35 gradually decreases with an increase of the electric frequency. The trace lengths in the left figure are used to calculate the electrophoretic mobility using Equation 27. The most striking difference is the large dependence of the measured mobility on the distance to the optical fibre. The measurements performed at 135 μm and 265 μm from the optical fibre have a much higher measured mobility than the particle tracks measured at a distance of 390 μm. The measurement at 5 V also has a lower measured mobility than the measurement of 7.5 V at the same distance.

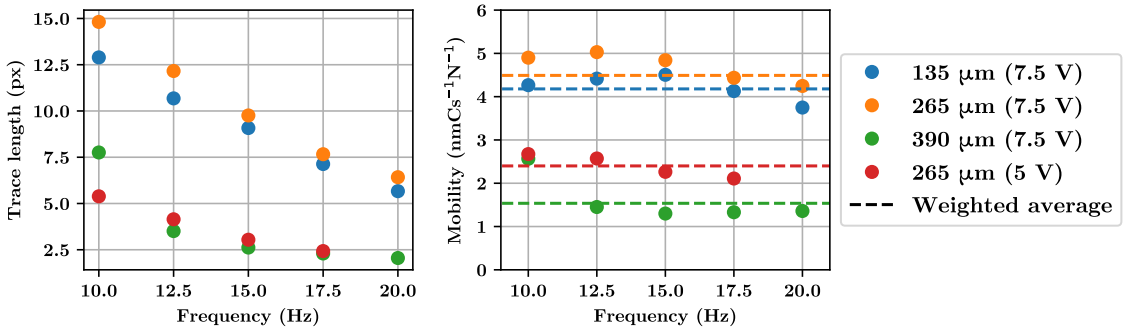

Figure 35: Results of the peak to peak height of the mean motion of all particles. In the left image the peak to peak length of the average movement in the y direction is shown. The average mobility of all frequencies for each distance is weighted with the number of detected particles. The trace lengths decrease with increasing frequency. These lengths are used to calculate the mobilities in the figure on the right, resulting in a small, but noticeable decay in electrophoretic mobility for each frequency. Most striking is the dependence on potential and distance.

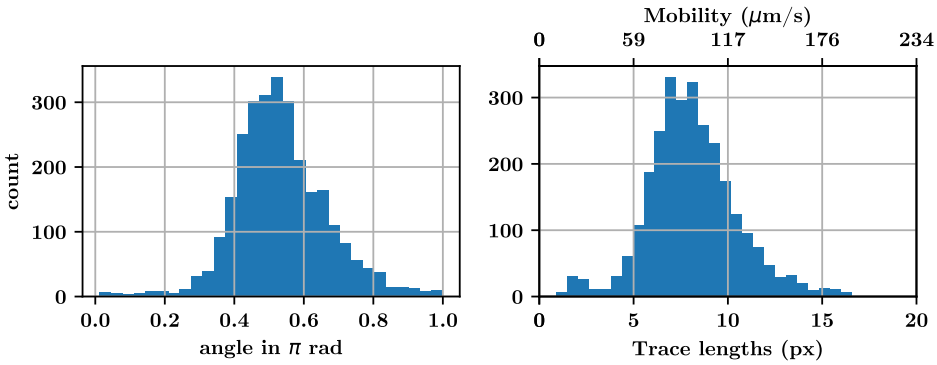

(a) 5.0 V at 10.0 Hz

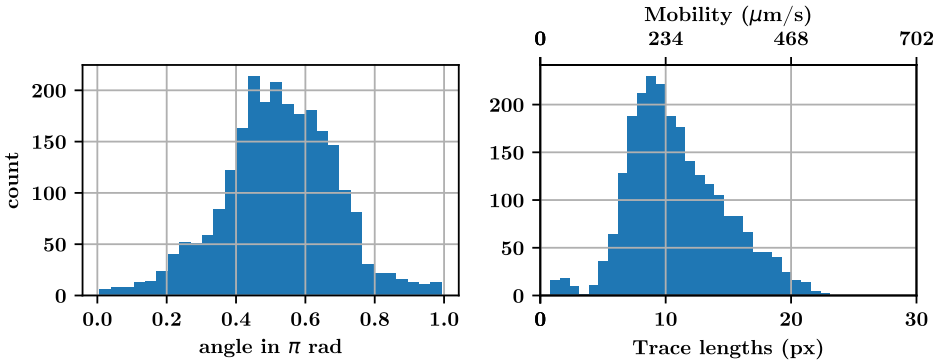

(b) 7.5 V at 20.0 Hz

Figure 36: Example of the length and angle distribution of two different measurements. The angle is the angle relative to the x axis. The electric field is in the y axis. The histograms at the right show a deviation from a Gaussian shape when a higher voltage is applied.

Calculating the ζ-potential from the reported values in Figure 35, gives about 6.3 mV for the two distances close to the fibre and 2.2 mV and 3.5 mV for the measurement at 390 μm and the measurement at 5 V, which is not nearly the expected ζ-potential in the range of 30 mV or 50 mV[26].

The differences between each measurement at each distance and the low measured ζ-potential may be caused by the influence of electro-osmotic flow caused by charge on the optical fibre. In the next section those possibilities are further explored by plotting the trace length distributions for different positions between the electrodes.

5.2 Analysis of the mobility distribution

For this technique to be able to separate different species and to give a measure on how accurate the mobility can be measured, the individual mobilities are measured. The trace length of the individual particles are calculated by the maximum distance between the detected locations of a particle in a video. This differs from the analysis of the collective motion were only movement in the y-axis was used. This means that the trace length is artificially higher due to drift in the x direction, but that the misalignment of the electrodes is taken into account, since not only the y direction is used for the calculation of the mobility. Two examples of the histograms of trace lengths are shown in Figure 36. Both angle histograms are roughly centred at 0.5π, which means that the particle traces are on average aligned on the y axis. What is remarkable of the histograms of the trace lengths is the skewness of the distribution at higher voltage. The distribution measured at a lower voltage is more symmetric than the histogram

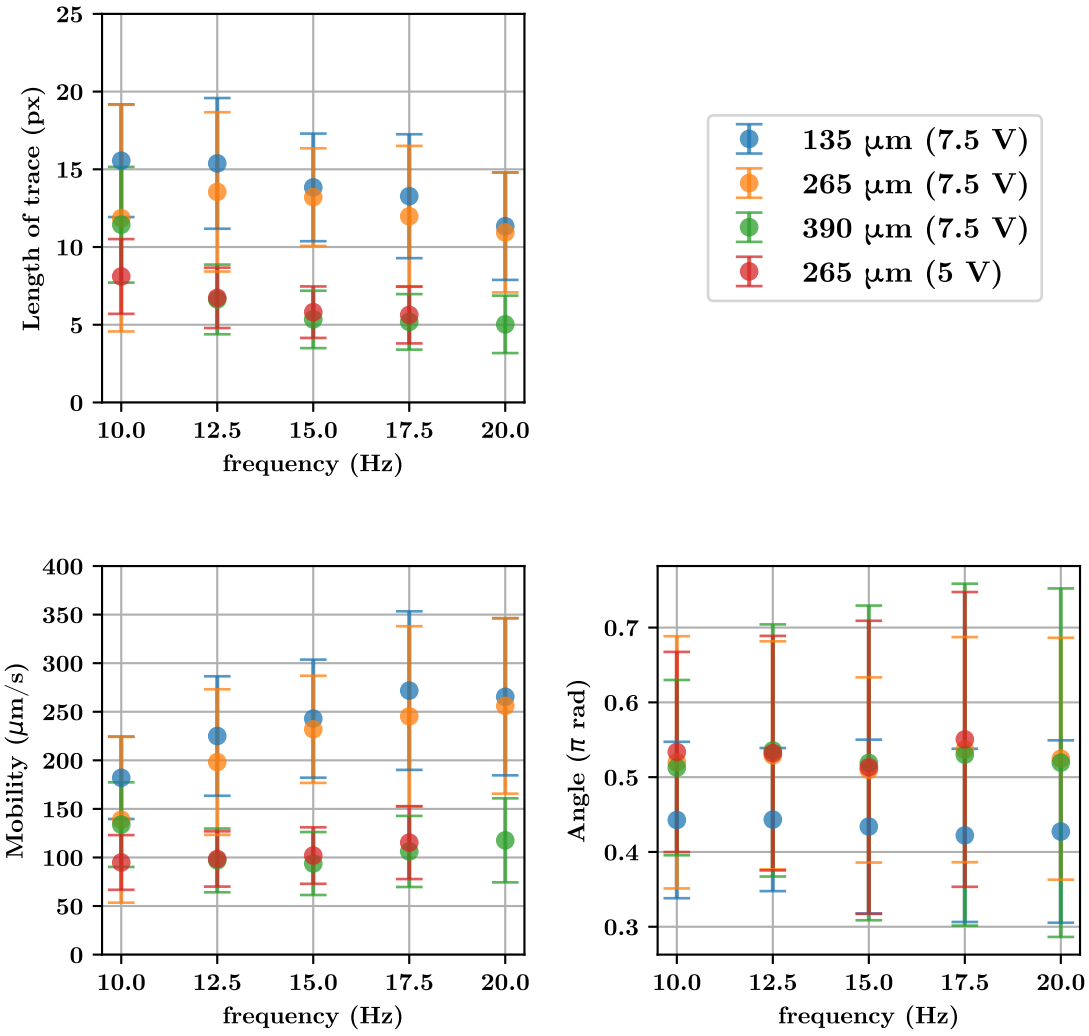

Figure 37: Summary of the results on the electrophoresis measurements for the three distances with different frequencies. The results of the experiments with lower potentials and with larger distance to the optical fibre are more consistent with the expected independence from the frequency of the potential. Closer to the fibre, the high frequencies have higher measured mobility.

of the higher voltage, because the distribution of the higher voltage has a tail towards higher trace lengths. The broad distributions are due to tracking errors, an inhomogeneous field and Brownian diffusion. The full length of a video is 0.17 s. The expected displacement due to Brownian motion for a 100 nm particle is 1.2 μm, which translates in this case to 3.2 pixels.

Because of the tail in the particle trace length distribution shown in Figure 36, the mean trace length may be biased towards a higher value. The median is less susceptible to outliers. In Figure 37 the trace length histograms are summarised. The bars are not error bars, but depict 68% of the population around the median, showing the range and skewness of the distributions. The median of the mobility distributions show a much larger dependence on the frequency than the mobility obtained from the average displacement. In the distributions for the measurements near the optical fibre, the measured mobility rapidly increases with the frequency. For the measurement at 265 μm the increase is about 30% from 10 Hz to 20 Hz. This behaviour is, however, not present at a larger distance from the fibre and at a lower electric potential of 5 V. The angle is a good sanity check, since the traces should be in the direction of the electrodes, which is 0.5π. This does not differ among the measurements except for 135 nm. The deviation

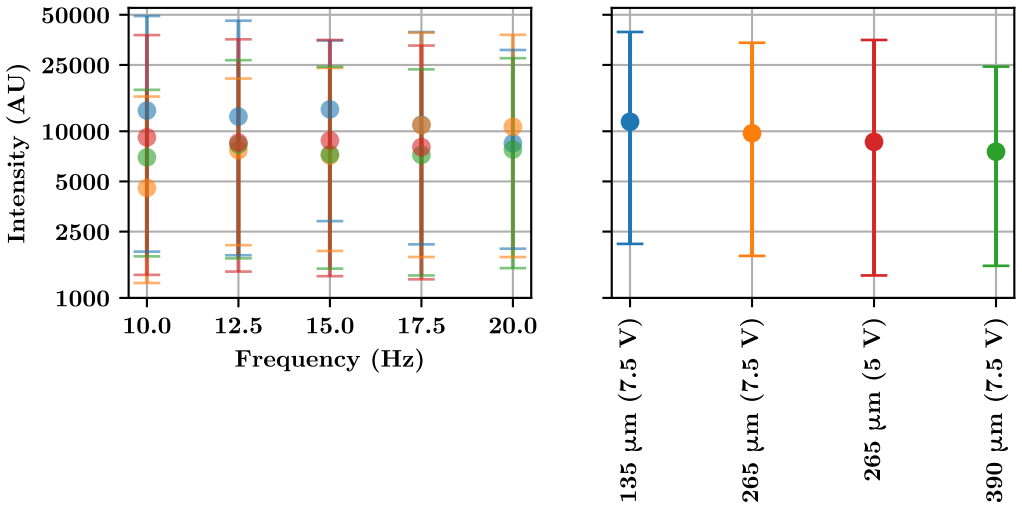

Figure 38: Median and a 68% interval of the intensities on a logarithmic scale. The difference in median intensity is considerable, but well within the spread of the intensity within each measurement.

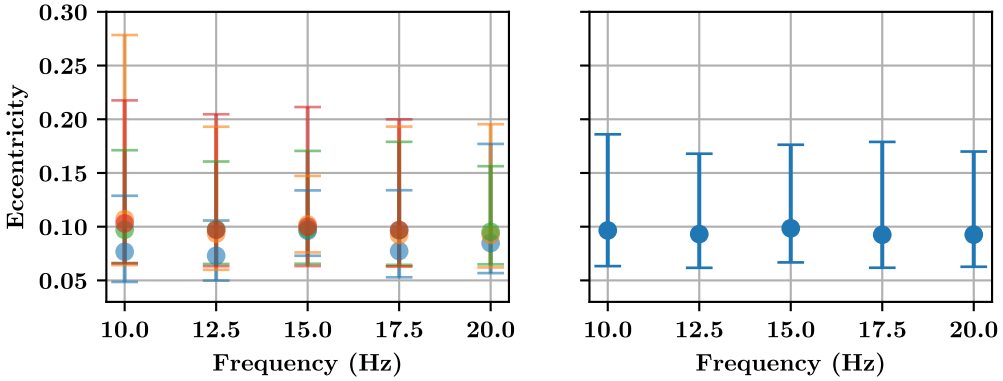

Figure 39: Mean eccentricities of the detected features. The mean eccentricities do not vary much among the measurements, with the exception of a lower mean and spread for the measurement close to the fibre. The eccentricity does not change with frequency. The same colours are used as in the previous graphs in this section.

between the measurements may be caused by errors in selecting the field of view, such that the window in which the particles are measured between the electrodes is at a slightly different location with respect to the electrodes. If a different part of the dipole field between the electrodes is imaged, the angle is off. The spread in the angle distributions is larger at higher frequencies. This is expected, because the shorter track lengths both have a larger error in the angle and the Brownian motion has more effect on the measured angle for shorter traces.

The particles at 390 μm receive a lower illumination intensity than the particles at 135 μm, because they are further from the fibre. In Figure 38 the the median and the 68% interval of the intensity distributions are plotted on a logarithmic scale. The intensity distribution varies greatly between measurements and have a high spread. The high spread in the distributions is to be expected, since the particles move in and out of focus. The intensities are higher for higher frequencies, probably because the particles have less motion blur, although this theory is not supported by the eccentricities of the particles in Figure 39, since the eccentricities of the detected features do not decrease for higher frequencies. The lower intensity of the

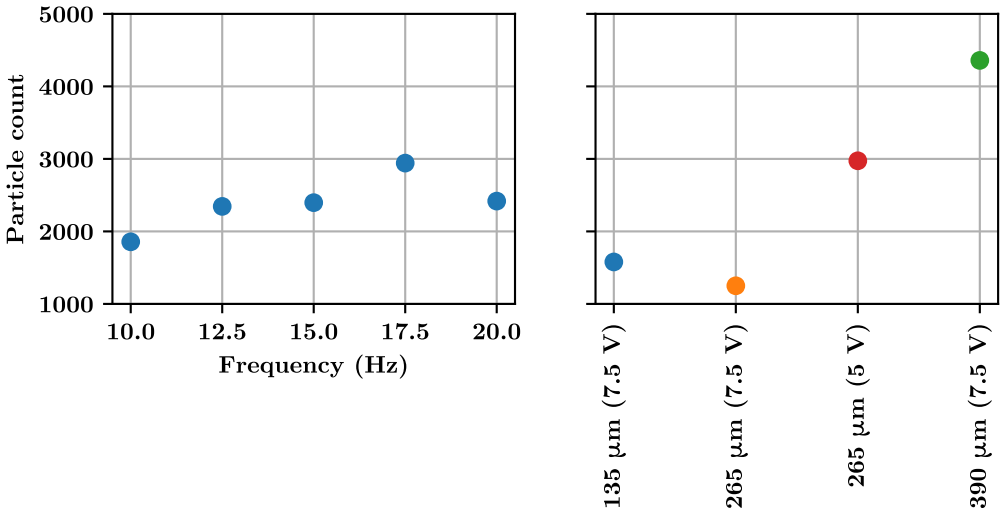

Figure 40: Mean particle count of each measurement for each frequency and distance. In the left image the average is over each distance measurement and in the left figure the averaging is over each frequency measurement. As expected the frequency does not influence the detection of the particles. The increase with higher distance is probably due to drying fo the droplet, since the measurement at 390 μm was measured last.

measurements at a distance of the optical fibre does not seem to hinder the detection of the particles, since the number of detected particles is the highest for the measurement the most distant from the fibre. The depth of focus is much lower than the width of the light cone of the laser light from the fibre, so particle count for the measurement at 390 μm is probably not due a larger illuminated volume. The measurement at 390 μm was measured last, so the increase in particle count is probably because of a higher particle density in the sample due to drying of the droplet. The electric frequency has no significant influence on the number of detected particles. This means that the faster moving particles are as well detected as the slower particles. The accuracy of the particle detection is higher with more signal, since both the mean eccentricity of the detected particle features and the spread is lower close to the fibre.

In Figure 41 the electric field between the electrodes is plotted and the number of detected particles is given as a heat map in the plots. With few exceptions the field lines do not quite resemble a dipole field. This is because the FOV was not entirely centred in the middle of the two electrodes for the measurements at 135 μm and 265 μm. The FOV with respect to the electrodes for those two measurements is shown in Figure 42. The number of detected particles is not dependent on the positions with respect to the electrodes: the space between the electrodes is used approximated equally. The deviations are caused by the low number of particles that are binned into the squares, since each measurement only consists of 100 videos of 20 frames.

Because the field lines deviate much at the edges of the FOV at 265 μm and at 135 μm, the angle is filtered to be within 0.4 π and 0.6 π for all measurements. In Figure 43 the effect of this filtering has been made visible by plotting all detected traces of the 17.5 Hz 7.5 V at 265 μm measurement. From these traces the field in Figure 41 (l) is calculated. Many traces are filtered out at the left side of the FOV and more reliable particle traces are retained in the centre of the FOV.

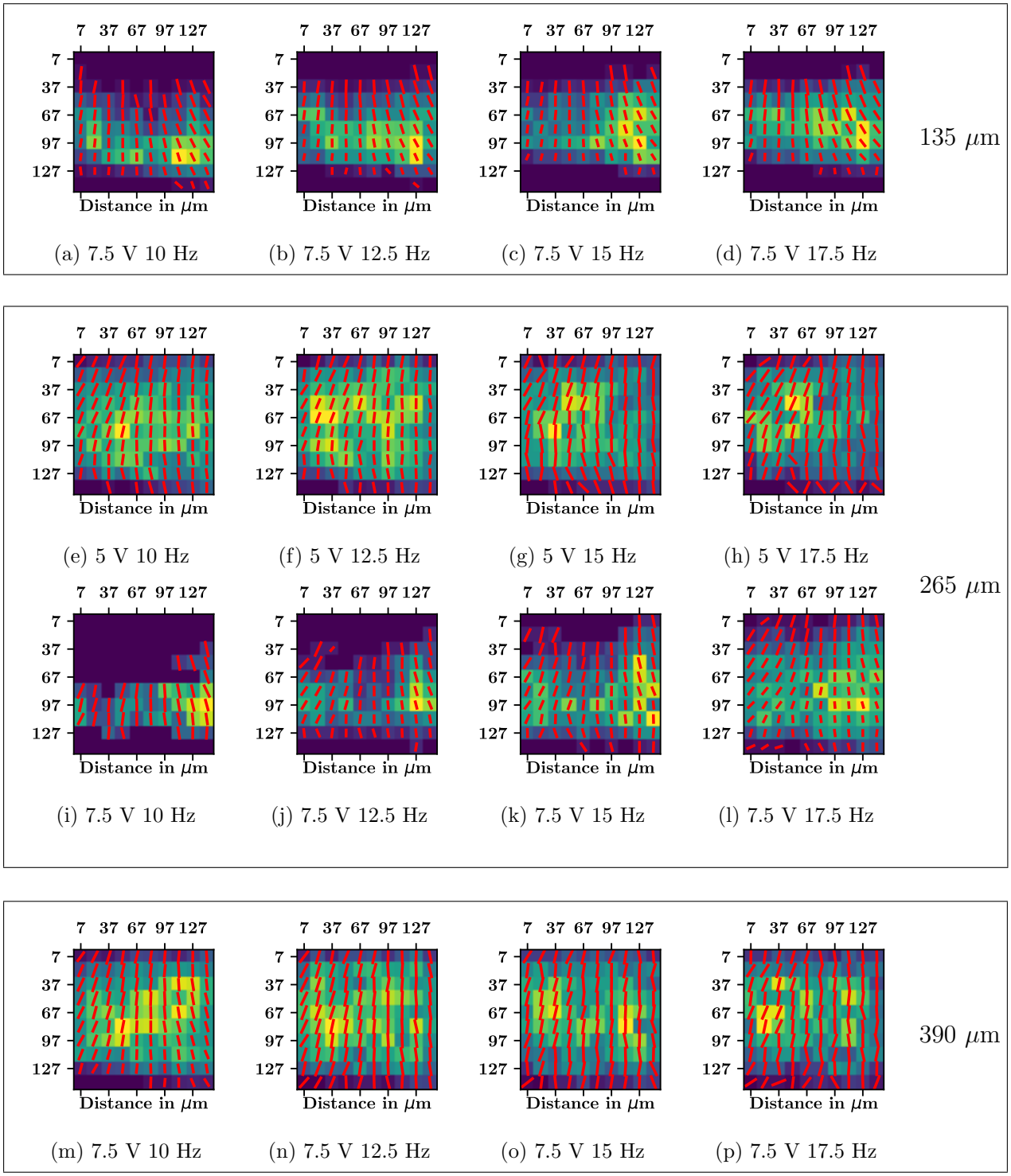

(a) 7.5 V 10 Hz (b) 7.5 V 12.5 Hz (c) 7.5 V 15 Hz (d) 7.5 V 17.5 Hz

(e) 5 V 10 Hz (f) 5 V 12.5 Hz (g) 5 V 15 Hz (h) 5 V 17.5 Hz

(i) 7.5 V 10 Hz (j) 7.5 V 12.5 Hz (k) 7.5 V 15 Hz (l) 7.5 V 17.5 Hz

(m) 7.5 V 10 Hz (n) 7.5 V 12.5 Hz (o) 7.5 V 15 Hz (p) 7.5 V 17.5 Hz

Figure 41: Length and direction of particle traces in the electic field measurements at different distances from the fibre. The red lines are pointed in the mean direction of the measured particle traces. The colour density denotes the particle count. In the blue the blue squares no traces are detected and in the yellow squares the most particles are detected. The length of the lines are proportional to the length of the detected particle track. The particle tracks should be along the electric field lines between the electrodes. The field is for each measurement relative homogeneous in the vertical direction, but on the sides of the measured area, the angles may differ a lot from 0.5π.

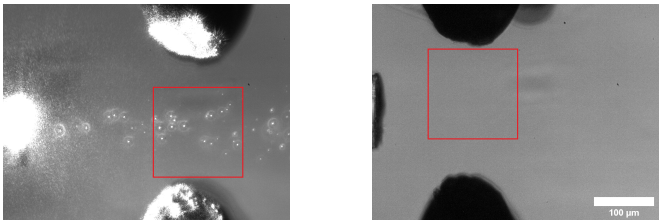

(a) 265 μm (b) 135 μm

Figure 42: The FOV is not centred for two distances. This causes the angle differences between the measurements. Filtering the angles that are not aligned with the electrodes gives a more homogeneous field.

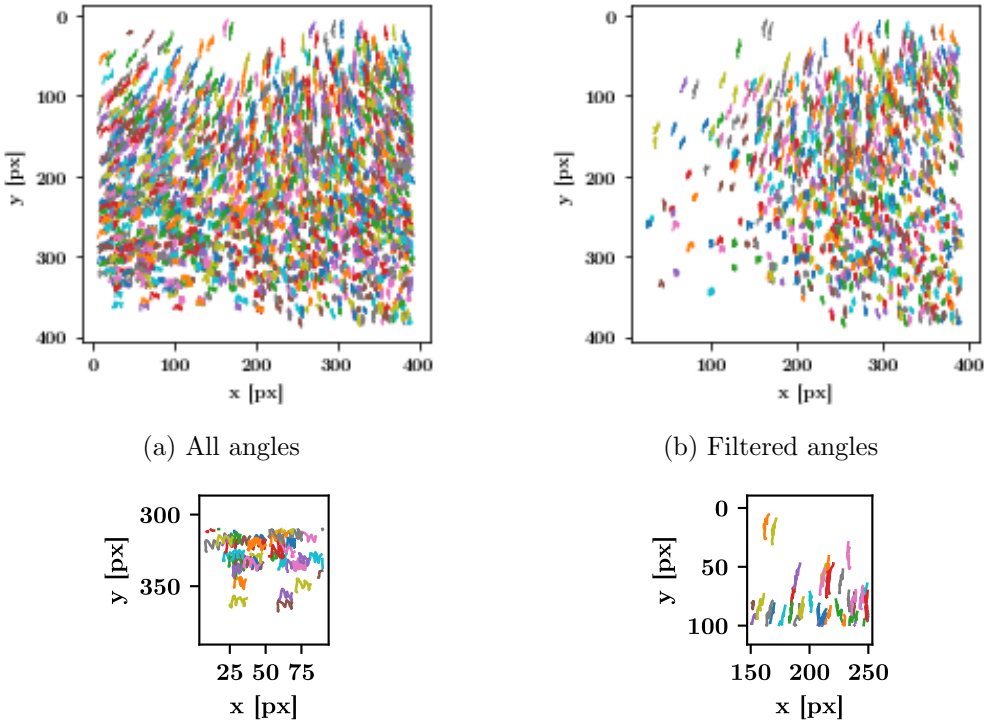

(a) All angles (b) Filtered angles

(c) Spurious traces in the corner. (d) Spurious traces near the electrode

Figure 43: Particle trajectories of the measurement at 265 μm, 7.5 V and 17.5 Hz. For the traces shown in Figure (b) spurious traces, except for those at the top of the image, near the electrode, are filtered out. In Figure (c) an example of spurious traces in the bottom left corner is shown. The traces show a clear drift in the x direction. In Figure (d) the traces are all in the y direction, but they have the same drift in the y direction, so the trace appear longer. This causes the frequency dependence in Figure 44 and Appendix D.

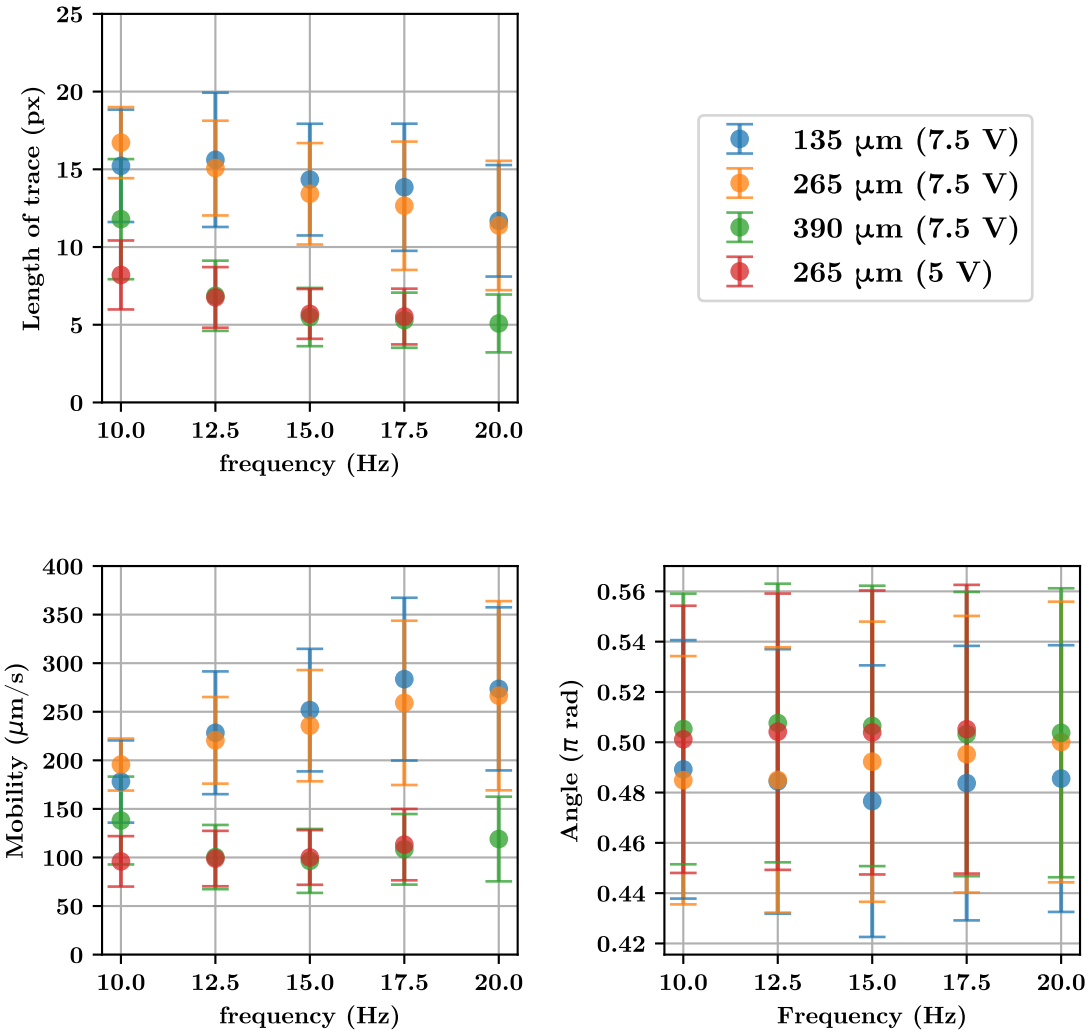

Figure 44: Trace lengths, mobility and angles after filtering of the angles. There are not many differences with the unfiltered results in Figure 37. The measurements at 135 μm and 265 μm still show a significant frequency dependence.

Examples of particle traces that are filtered out by the angle requirement are shown in Figure 43 (c). On top of the motion in the y direction, the direction of the electric field, the particles move in the x direction. This drift is present in each particle in that part of the FOV. Each particle in that area of the FOV has approximately the same shape. This shape is not present in other areas of the FOV, so this is not a general drift of all particles during the measurement. The same behaviour, but in the x direction is visible at the top of the particle traces. The particles have a different response to the positive part of the sinusoidal AC potential that the negative part of the potential, causing a resultant motion in the negative y direction over the course of a few AC cycles.

The filtered results are plotted in Figure 44. Apart from minor changes, the frequency dependence of the measurements at 135 μm and 265 μm is still considerable, but the features as Figure 43 (d) are still present, because they align with the electrodes in the y direction. The results in Figure 35 are corrected for the drift. According to the average movement in Figure 45 the drift is about 2 px which is about the same as the discrepancy between the pixel lengths of the traces reported in Figure 44 and Figure 37.

The traces in Figure 43 exhibit a complicated motion in the electric field with features like Figure 43c and 43 (d) at different positions with respect to the electrodes. The measurements

were performed a few 100 μm from the microscope slide and af few 100 μm from the optical fibre. These distances are short enough that the charge of the surfaces could influence the motion of the liquid by electro-osmosis. The measured particle motion therefore has both an unknown electro-osmotic part on top of the electrophoretic mobility of the particle. Since both the charge on the microscope slide, the charge on the fibre and the ion distribution in the liquid all contribute to the electro-osmotic flow, the resultant motion can be complicated and position dependent. The flow is governed by the modified Navier-Stokes equation (Equation 21), which also contains the continuity and time dependence of the liquid flow. This means that a system that is not symmetric, as assumed in Section 2.5, has a liquid flow in all 3 directions. Since the electrodes, the fibre and the microscope slide impose their own boundary conditions on the flow, the complicated electro-osmotic part can only be decreased if the measurement is performed on a large enough distance from all charged surfaces.

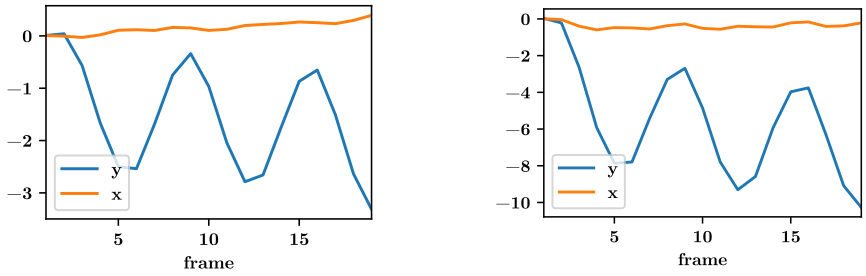

(a) 5 V, 17.5 Hz

(b) 10 V, 17.5 Hz

Figure 45: The angle filtered drifts. There is still an overall trend in the average particle movement due to the motion of the particles shown in the tracks of Figure 43 (d).

The median trace lengths and mobilities for only the first period of the AC wave are shown in Figure 46. The measured trace lengths and the mobilities are in accordance with the average motion in the y direction. This means that the frequency dependence of earlier measurements reported in Appendix D are probably due to drift in the fluid itself caused by electro-osmosis, since a charged particle alone cannot describe the motion of a trace like the one shown in Figure 43 (c) and 43 (d). The large difference between the distances and the lower potential remain. This means that the effect of the charge the optical fibre is still significant. Both electrophoresis and electro-osmosis should be linear in the applied potential, but the trace lengths of the measurement at 5 V is much lower than would be expected from linear behaviour.

The fields without features similar to the traces shown in Figure 43 (c) are plotted in Figure 47. The distribution of particle densities changed for the two measurements in which the x position of the FOV was misaligned, but the fields are almost vertical between the two electrodes. The traces are longer, when they are closer to the electrodes. The filtered field between the electrodes is relatively independent on both the x and y positions, which means that the shape of the electrodes was reliable enough to perform measurements and that the electro-osmotic flow is approximately constant, such that the measurement of the electrophoretic mobility of particles is a matter of calibration with particles with a known ζ-potential. This is something that is not uncommon in electrophoresis experiments[16]. Comparison between particles with different charge should be possible when imaged in the centre of the electrodes, both in te x and in the y direction.

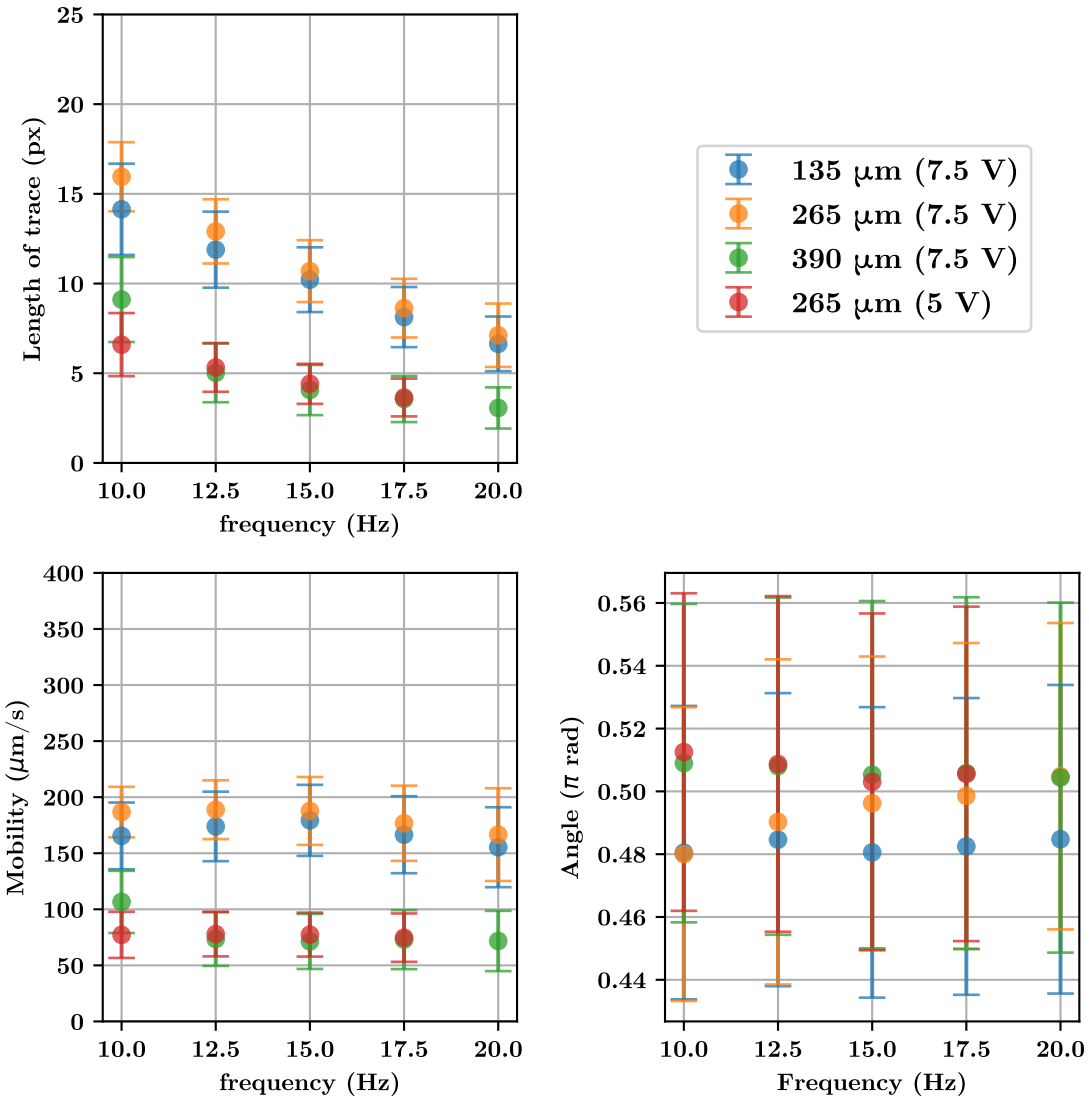

Figure 46: Trace lengths, mobility and angles after filtering out both the angle in a different direction as the electrodes and taking only the first period of the AC electric potential . The frequency dependence is gone, which means the fluid flow in the y direction caused the frequency dependence in Figure 37 and 44 and Appendix D. The trace lengths are now in accordance with the trace lengths reported in Figure 35.

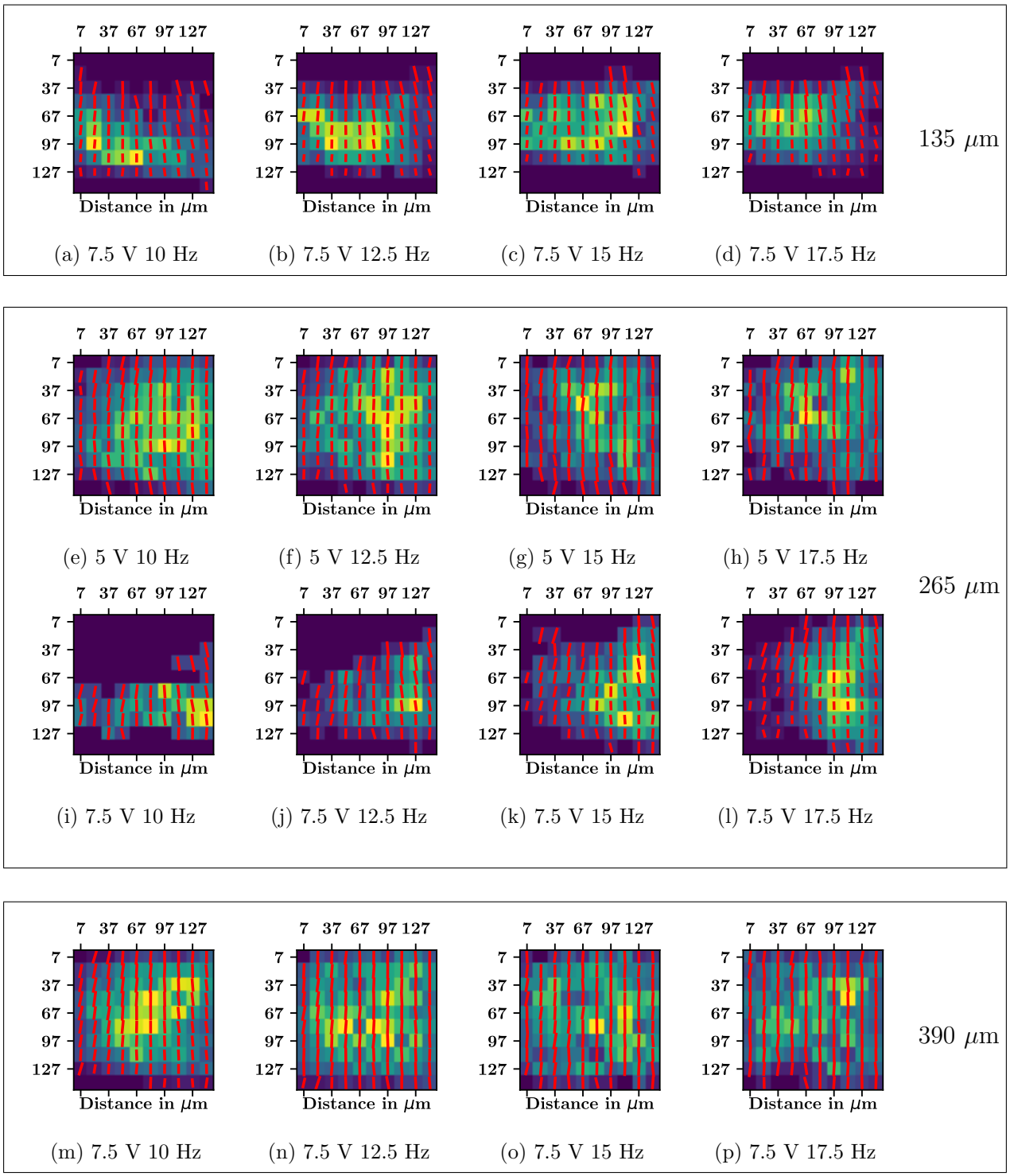

(a) 7.5 V 10 Hz (b) 7.5 V 12.5 Hz (c) 7.5 V 15 Hz (d) 7.5 V 17.5 Hz

(e) 5 V 10 Hz (f) 5 V 12.5 Hz (g) 5 V 15 Hz (h) 5 V 17.5 Hz

(i) 7.5 V 10 Hz (j) 7.5 V 12.5 Hz (k) 7.5 V 15 Hz (l) 7.5 V 17.5 Hz

(m) 7.5 V 10 Hz (n) 7.5 V 12.5 Hz (o) 7.5 V 15 Hz (p) 7.5 V 17.5 Hz

Figure 47: Field between the electrodes when the angles are filtered to be in the direction of the electrodes. The squares at 135 μm and 265 μm that had very skew traces in Figure 41 are now almost empty, because they have been filtered out.

6 Outlook

One of the problems of using single particle tracking for diffusing particles to obtain the size distribution is the unreliability of the results of the particles that could only be imaged for a short time, as supported by computer simulations. The time the particle is in focus can be increased with low NA objectives at the cost of resolution. An easier method to increase the number of frames in which a particle is detected is to use a camera with a higher frame rate. Increasing the FPS of the camera is at the cost of signal. The best results are by using a high NA objective with a high speed camera and a strong illumination. Since this is not always possible, it is a trade-off between these parameters.

In this work the diffusion of a particle in the optical axis is considered as the biggest limiting factor of obtaining many data points of the same particle. The position in the optical axis of the particle is not used to refine the measured diffusion coefficient. This diffusion of the particle in the optical axis could also be used as an advantage by using the PSF of the particle to determine the position in the z axis. The method used by Huang *et al.*[27] makes uses use of diffusion in the optical axis by using a cylindrical lens, so the position of a particle can be measured by the shape of the PSF.

The intensity of the scattered light from the particles is more sensitive to the diameter (a^6) than the diffusion constant (a^{-1}). In this experiment the differences in intensity were mostly due to differences in the z position. If the particles could could be confined the intensity of the particles could be used to obtain the diameter distribution by both diffusion and intensity of the scattered light. In this project an attempt was made to confine the particles, but without success, see Appendix C. Confinement of the particle allows for much more frames per particle. Faez *et al.*[5] uses confinement to measure particle sizes of particles smaller than used in this project.

The disaggregation of the tau fibrils has now taken place outside of the measurement apparatus. The samples were frozen after a number of hours. This setup can be used to measure the disaggregation process real-time. Since the disaggregation of the fibrils should take place at 37° C, the sample could be heated during measurement of the real time disaggregation. Because the sample would evaporate on the time scale of 24 h an open channel, as used in this project cannot be used. The channel needs to be closed such that a long measurement can take place.

The research presented in this thesis has shown that measuring the electrophoretic mobility of nanoparticles can be non trivial. The influence of the charge of fibre and the microscope slide can be further investigated by varying the potential and the distance between the electrodes and by varying the distance between the microscope slide and the electrodes. Since the distance between the electrodes and the fibre has a large influence on the measured mobility of the particles, the distance between the electrodes themselves and the distance between the electrodes and the microscope slide should also have an effect on the measured electrophoretic mobility of the particles. Measuring the response of particles in an electric field between manipulable electrodes can be an easy method to determine the mobility of the particles, provided that reliable parameters can be found to measure the electrophoretic mobility in a more quantitative way, than the measurements in this project.

7 Conclusion

Tracking of diffusing nanoparticles can be used to measure their size. The Brownian motion of gold nanoparticles with an unknown polydispersity with a diameter of 30 nm and 40 nm was tracked. The obtained diameter distributions were broad and asymmetrical giving a mean diameter of 31.8 nm, 53.2 nm and 66.0 nm for 30 nm particles, 40 nm particles and a mixture of both. Because of a long tail in the diameter distribution towards largerm diameters, the median size is a better quantity to describe the particle size in a single number. The median particle sizes are 21.3 nm, 33.3 nm and 25.2 nm for 30 nm particles, 40 nm particles and the mixture. Although the measured distributions are broad, the particles themselves could be well detected by the laser illumination from the side.

The broad particle distributions are mostly due to a limited number frames in which particles are detected. Tracking of simulated data of Brownian diffusing particles measured with finite camera exposure time show that particle tracks lower than 30 frames cannot be reliably fitted to the Stokes-Einstein equation to determine the size. Not only the spread in the detected MSD is much larger for measurements with only a few frames, but there is also a systematic error towards a artificially higher measured MSD.

Single particle tracking is used to find changes in the size distribution in a disaggregation process of tau fibrils by molecular chaperones. The particles that are the product of the disaggregation of the particles are tracked in 7 samples in which the chaperones could react with the fibrils for 0, 4, 8, 9, 16, 20 and 24 hours. These particles have a size of about 100 nm, if the particles would be spherical. In 24 h the size distribution of the particles in the sample decreased and the number of detected particles increased, suggesting that the tau fibrils are broken down by the molecular chaperones.

The electrophoretic mobility of 100 nm gold nanoparticles is measured at different distances from the optical fibre. The distance to the optical fibre has a great effect on the response of the nanoparticles on an electric field. This deviation from simple linear behaviour is probably caused by an electro-osmotic flow with a longer damping time than the period of the applied AC potential. Using a naive calculation using the Helmholtz–Smoluchowski equation (Equation 20) without taking the flow or capacitance of the water into account the ζ-potential of the particles is 6.3 mV at a distance to the optical fibre of 135 μm and 265 μm and 2.2 mV at a distance of 390 μm. Since this is much lower than the typical ζ-potential of gold nanoparticles, this method of measuring the electrophoretic mobility of particles must be calibrated with a particle with a known ζ potential. The field between the electrodes is between the tips approximately homogeneous. Only when measured on a larger distance from the electrode the field looks like a dipole field, so no correction is needed for an inhomogeneous field for the particles in the centre of the electrodes. Particles that deviate from the centre have a complex motion that includes both electro-osmosis and electrophoresis.

8 Acknowledgements

For making the writing of this thesis possible I would like to thank my supervisor Sanli Faez. He did not only made it possible for me to do my research project at the Nanolinx group, but he also helped me on various occasions when the experimental work did not go along the straight path to results that I hoped it would go. I also would like to thank Allard Mosk for being the second reader of my thesis and also for that I could do my this project at the Nanolinx group. More specifically I would like to thank Allard because he made me go to the EOSAM conference, which was a nice experience.

I would like to thank Gerarda van de Kamp, because she provided me with her tau fibrils and worked patiently with me to measure the disaggregation process. An entire section of my thesis is based on her fibrils. I therefore also thank Sanli Faez and Stefan Rüdiger for making this collaboration possible.

My daily supervisor Dashka Baasanjav gets my thanks for helping me in the lab and helping me in the crunch hours just before the EOSAM conference. Along with Dashka I would like to thank Bohdan Yeroshenko for being an unofficial daily supervisor and for his helpful discussions about my project, but also the conversations that were not about my project. In the summer, when most of the people of Nanophotonics were gone, Aquiles Carattino could help me with my experiment and with my programming, but most of all, my coding habits. I would like to thank him for these helpful discussions.

I would like to thank Lorenzo Sierra Perez for the month I worked with him when we both started our projects together and for various helpful discussions. Tang Qianjing (or Qianjing Tang) also deserves my thanks for being a nice guy to work with in the lab.

This thesis could not be written without Mijke Heldens and the technical staff of Nanophotonics, so I would like to thank them all. Especially Cees de Kok whose office I visited a lot for important lab equipment like sticky tape. I would like to thank Dante Killian for his technical assistance and Paul Jurrius for milling and tapping my flow cells and sample holders.

I also would like to thank Rachel Armstrong from the TU/e for her time explaining me about particle conjugates, although, unfortunately, I was not able to go to Eindhoven for the particle conjugate experiment.

Of course I thank all the people of the Nanophotonics group, because in the year I did my project in this group, everybody gave me advice in one way or the other.

References

[1] H. Bruus. *Theoretical Microfluidics*. Oxford University Press, 2008.

[2] P. Nakroshis, M. Amoroso, J. Legere, and C. Smith. Measuring boltzmann's constant using video microscopy of brownian motion. *Am. J. Phys*, 71(6):568–574, 2002.

[3] J. Perrin. Mouvement brownien et réalité moléculaire. *Annales de Chimie et de Physique*, 18:4–113, 1908.

[4] V. Filipe, A. Hawe, and W. Jiskoot. Critical evaluation of nanoparticle tracking analysis (nta) by nanosight for the measurement of nanoparticles and protein aggregates. *Pharm. Res.*, 27(5):796–810, 2010.

[5] S. Faez, Y. Lahini, S. Weidlich, R.F. Garmann, K. Wondraczek, M Zeisberger, M.A. Schmidt, M. Orrit, and V.N. Manohara. Fast, label-free tracking of singleviruses and weakly scatteringnanoparticles in a nanofluidicoptical fiber. *ACS Nano*, 9(12):12349–12357, 2015.

[6] R. Westermeier. Gel electrophoresis. *encyclopedia of Life Sciences*, 2005.

[7] T. Thorsen, S. Maerkl, and S. Quake. Microfluidic large-scale integration. *Science*, 298 (5593):580–584, 2002.

[8] S. Balslev, A. Jorgensen, B. Bilenberg, K. Mogensen, D. Snakenborg, O. Geschke, J. Kutter, and A. Kristensen. Lab-on-a-chip with integrated optical transducers. *Lab Chip*, 6(5):213–217, 2006.

[9] J. Cybulski, J. Clements, and M. Prakash. Foldscope: Origami-based paper microscope. *PLoS One*, 9(6):e98781, 2014.

[10] A. Einstein. Über die von der molekularkinetischen theorie der wärme geforderte bewegung von in ruhenden flüssigkeiten suspendierten teilchen. *Annalen der Physik*, 322(8):549–560, 1905.

[11] A.P. Philipse. Brownian motion, lecture notes, 2017.

[12] R. van Roij. Soft condensed matter theory, lecture notes, 2010.

[13] X. Michalet. Mean square displacement analysis of single-particle trajectories with localization error: Brownian motion in an isotropic medium. *Phys. Rev. E*, 82(2):041914, 2010.

[14] D.S. Martin, M.B. Forstner, and J.A. Käs. Apparent subdiffusion inherent to single particle tracking. *Biophys. J.*, 83(4):2109–2117, 2002.

[15] H. Qian, M.P. Sheetz, and E.L. Elson. Single particle tracking: Analysis of diffusion and flow in two-dimensional systems. *Biophys. J.*, 60:910–921, 1991.

[16] A.V. Delgado, F. Gonzàlez-Caballero, R.J. Hunter, L.K. Koopal, and J. Lykema. Measurement and interpretation of electrokinetic phenomena. *J. Colloid Interface Sci.*, 309: 194–224, 2007.

[17] J. Seinfeld and N. Pandis. *Atmospheric Chemistry and Physics, 2nd edition*. John Wiley and Sons, 2006.

[18] G. Wang and C.M. Sorensen. Experimental test of the rayleigh-debye-gans theory for light scattering by fractal aggregates. *Appl. Opt.*, 41(22):4645–4651, 2002.

[19] T. Savin and P.S. Doyle. Static and dynamic errors in particle tracking microrheology. *Biophys. J.*, 88(1):623–638, 2005.

[20] N. Bobroff. Position measurement with a resolution and noise-limited instrument. *Rev. Sci. Instrum.*, 57(6):1152–1157, 1986.

[21] ThorLabs. Product data sheet, single mode fiber-pigtailed laser lp405-sf30, 2016.

[22] Basler. Product documentation, daa1280-54um, (version 14), 27 June 2018.

[23] G. van de Kamp. *Tau fibrils bind essential cellular proteins via pi-interactions and are disaggregated by human molecular chaperones.* Universiteit Utrecht, 2018.

[24] J.C. Crocker and D.G. Grier. Methods of digital video microscopy for colloidal studies. *J. Colloid Interface Sci.*, 179(217):298–310, 1996.

[25] D. Allan, T.A. Caswell, N. Keim, F. Boulogne, R.W. Perry, and L. Uieda. trackpy: Trackpy v0.2.4, 2014.

[26] M. R. Ivanov, H.R. Bednar, and A.J. Haes. Investigations of the mechanism of gold nanoparticle stability and surface functionalization in capillary electrophoresis. *ACS Nano*, 3(2):386–394, 2009.

[27] B. Huang, W. Wang, M. Bates, and X. Zhuang. Three-dimensional super-resolution imaging by stochastic optical reconstruction microscopy. *Science*, 319(5864):810–813, 2008.

[28] Basler. Pypylon, 2018. URL `https://github.com/basler/pypylon`.

A Python Scripts

The data acquisition scripts and the scripts that calculate the particle tracks from a time stack of frames in the HDF5 format are accessible on-line at:

`https://github.com/nanoepics/CETgraph/tree/peter`

The repository includes the following scripts:

- `autoCropper.py`: This script uses image processing techniques described in the methods section to obtain particle tracks from images with a long exposure time. This script was not used for the main results in this thesis.
- `camera.py`: This script uses Pypylon[28] to access the camera. It runs the camera with predefined settings and saves the data as AVI and HDF5 files. It also calls the background subtraction script `subtractBackground.py`.
- `setMassBoundaries.py`: This script opens the first frame of a imaged stack and displays the detected features for user defined settings.
- `simulateBrownianMotion.py`: This script contains the `simulateBrownianMotion` class that simulates the data of a diffusing particle.
- `simulateBrownianMotionExample.py`: This script creates an `simulateBrownianMotion` object and handles the output of the simulation.
- `subtractBackground.py`: This script subtract the background of an imaged stack of moving particles with a static background.
- `traceClicker.py`: This script allows the user to select particle features. This script was not used for the main results in this thesis.
- `track.py`: This script locates particles, links the features into tracks and saves the tracks together with its diameter, total intensity, eccentricity and diffusion constant.
- `trackParticles.py`: This script performs IO for `track.py`.
- `trackUtils.py`: Static class for IO and plotting for different Python scripts.

The scripts that use the particle tracks obtained from these scripts for plotting are stored with the data.

B Trace detection

In this appendix some results on the linear fits are shown. For the main results the analysis of videos is used, due to the problems described in this section. The videos also have an advantage that drift in the sample can be detected by means of the average motion of the particles. This is not possible with the linear fits of particle traces.

Following the process described in Section 3.5.3, particle traces are cropped from the image. In Figure 48 the result is shown. The features in the mask in Figure 48b are filtered based on minimum brightness, distance to the wall and minimum and maximum intensity. Examples of two detected features is shown in Figure 49. Both the left and the right images satisfied the conditions that were imposed to retain the features as a particle trace. The number of false positives as in Figure 49b was too high to use the cropping script to obtain data from the exposed images.

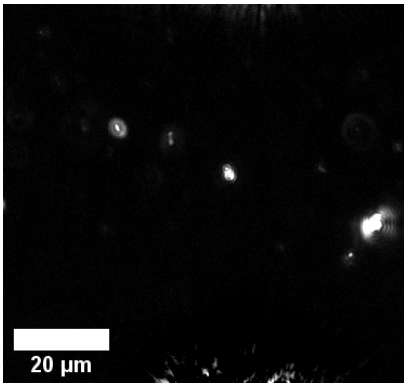

(a) Long exposed image with particle traces.

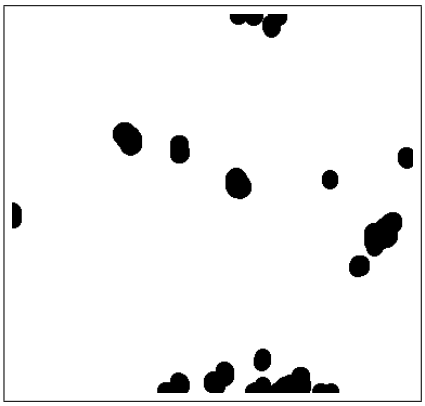

(b) Mask

Figure 48: The features in the left image are detected. The brightness is increased for better visibility. The mask overlay in the right image shows all candidate pixels. The black parts of this mask are all candidate features. The spurious features caused by the scattering from the electrodes were filtered out, so the features at the top and bottom were recognised as light electrodes.

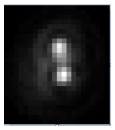

(a) Correctly identified particle

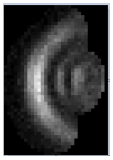

(b) Part of an Airy disk, wrongly identified as particle

Figure 49: Particles detected by the method described in Section 3.5.3. The left particle feature is correctly detected as a particle, whereas the right image is a bright particle that is out of focus.

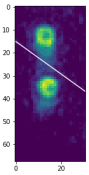

(a) Linear fit

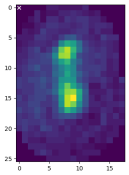

(b) No local maxima found

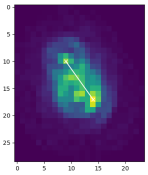

(c) Correct fit between the tips

Figure 50: Different methods to fit to detected particle traces. Both the linear fit and the connection of the local maxima generate too much false positives.

Using the `traceClicker.py` script from Appendix A the traces can be manually selected, if the `autoCropper.py` script would fail. To obtain the length of the particle traces two methods were tried: a linear fit with the pixel values as weights for the fit and detection of local maxima similar to how the Trackpy package detects local maxima. Because the particles spend more time at the tips of the traces if a sine wave is applied, there are two local maxima at the tips of the trace. The largest distance between the maxima was chosen if more than two local maxima were found. The linear fit was able to find a fit in only very few cropped particle traces, while the traces are too noisy and the tips of the traces too close together to find two local maxima. Examples of these fits are plotted in Figure 50. Because of these difficulties the measurements on the electrophoretic mobility was done by single particle tracking in videos.

C Confinement of nanoparticles

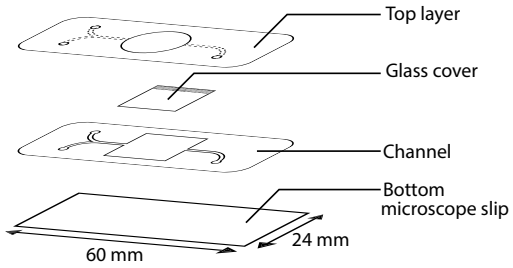

Figure 51: Sketch of the flow cell. The water inlets are in the top layer. The particles that are imaged are underneath the 15×15 mm^2 cover. The microscope objective is at the bottom.

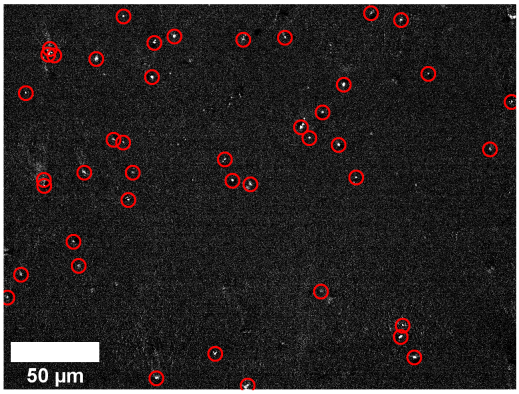

Figure 52: Located particles. Note the high background scattering and low SNR.

To prevent the particles from moving in and out of focus the particles were confined in a microchannel made by laminating plastic and a spacer of stretched parafilm. Because the channel is very thin, the channel was illuminated from the top instead of the side. The scattering on the glass cover and the bottom microscope slip proved to be too large to be able to perform reliable particle tracking.

For the imaging two samples are used. One sample is made with a channel and two cover slips. The bottom is a 60×24 mm^2 #1 microscope cover slip. The channel is cut out from laminating plastic. The plastic has about the same thickness as the cover slips. In the channel a 15.25×15.25 mm^2 square is left out for a glass cover. The 15×15 mm^2 cover has at the bottom a thin strip of stretched out parafilm attached to it as a spacer. The particles that are imaged are between this cover and the bottom microscope slip. The parafilm strip is stretched until it stretches no further. Because the parafilm strip is attached to only one side of the 15×15 mm^2 cover, the thickness of the channel increases from the side without parafilm attached to the parafilm side. To seal the channel a plastic top layer made out of laminating plastic. The plastic cover has a 13 mm circle cut out to make it possible to image through the glass cover. Holes are made as in- and outlets for the liquid. The EVA coating above the channel is removed from the top layer to prevent blocking of the channel. Both plastic layers have their EVA coating on the bottom side, so no gluing is required. The layers are put together and laminated with a laminating machine. Imaging can be done through both cover slips, but is done through the bottom cover, to make it possible to let fluids in from the top layer.

For the other sample the plastic channel is left out. This simpler sample consists of two microscope slips. The bottom slip is a #1 60×24 mm^2 cover slip and the upper cover slip is a #1 15×15 mm^2 cover slip. A parafilm spacer is attached to one of the sides of the 15×15 mm^2

cover. The side without parafilm is glued with viscous UV glue to prevent the glue form creeping into the sample.

The flow cell is placed into a acrylic glass holder. The holder has inlets at the three holes in the flow cell. The holes are connected with tubes through which air can be sucked or pushed. The laser light enters the sample with an angle of approximately 120°. Most of the laser light reflects on the surface of the top cover slip, but a fraction of the laser light scatters on the particles. The scattered light is detected by an objective lens and imaged by a camera. In the channel with the stretched parafilm spacer all light goes through glass. In the simple plastic channel a typical image looks like the image shown in Figure 53. The light that is scattered on the plastic is indistinguishable from the scattered light from the particles. Analysis of the tracks of particles imaged in the plastic channel would rely too much on background subtraction.

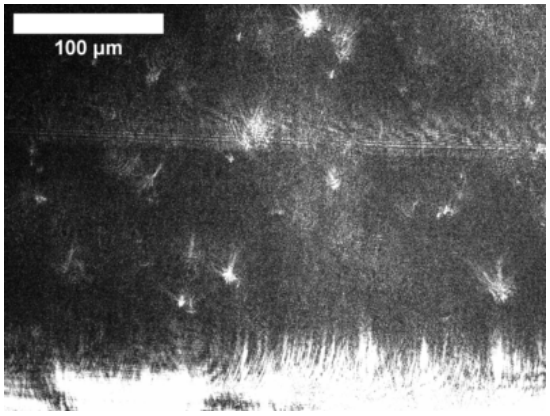

Figure 53: Scattering with a plastic channel. The 100 nm gold nanoparticles are indistinguishable from the scattered light from the plastic.

D Fixed Electrodes

The results of the measurements with the fixed electrodes are shown in Figure 54. The trace lengths and the mobility show a larger frequency dependence. The frequency dependence is due to the flow of the liquid as described in Section 5. The measured mobility is much lower than obtained with the manipulable platinum electrodes. The shape and alignment were bad compared to the manipulable electrodes, since the manipulable electrodes were much better to align.

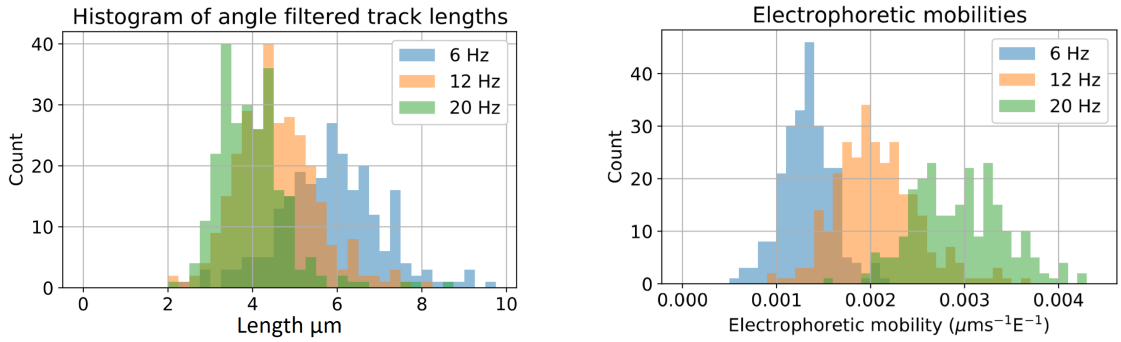

(a) Trace lengths

(b) Mobilities

Figure 54: The measured trace lengths and electrophoretic mobilities of 100 nm GNPs measured with the fixed copper electrodes.

E Violin plot size distribution tau fibrils

In this violin plot the size distributions that are plotted in the box plot in Figure 31 are shown.

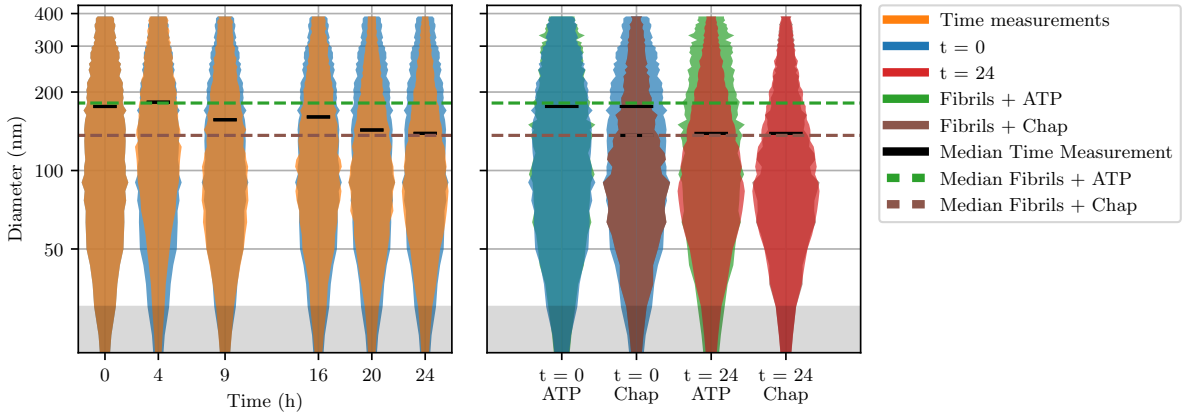

Figure 55: Logarithmic violin plot of the particle diameter distributions of the time measurements and the $t = 0$ and $t = 24$ sample compared with the two control samples. The diameter distribution of the $t = 0$ sample looks very similar to the sample with fibrils and ATP and the diameter distribution of the $t = 24$ sample looks similar to the control sample with ATP and chaperones. The area of diameters below 30 nm is greyed out, because the particle tracking is not reliable in this area.